HHS Public Access

Author manuscript

Med Image Anal. Author manuscript; available in PMC 2018 August 01.

Published in final edited form as:

Med Image Anal. 2017 August ; 40: 154–171. doi:10.1016/j.media.2017.06.007.

A New Algebraic Method for Quantitative Proton Density Mapping using Multi-Channel Coil Data

Dietmar Cordes[1,2,*], **Zhengshi Yang**[1], **Xiaowei Zhuang**[1], **Karthik Sreenivasan**[1], **Virendra Mishra**[1], and **Le H. Hua**[1]

[1]Cleveland Clinic Lou Ruvo Center for Brain Health, Las Vegas, Nevada, USA

[2]University of Colorado, Boulder, Colorado, USA

Abstract

A difficult problem in quantitative MRI is the accurate determination of the proton density, which is an important quantity in measuring brain tissue organization. Recent progress in estimating proton density in vivo has been based on using the inverse linear relationship between the longitudinal relaxation rate T_1 and proton density. In this study, the same type of relationship is being used, however, in a more general framework by constructing 3D basis functions to model the receiver bias field. The novelty of this method is that the basis functions developed are suitable to cover an entire range of inverse linearities between T_1 and proton density. The method is applied by parcellating the human brain into small cubes with size 30mm × 30mm × 30mm. In each cube the optimal set of basis functions is determined to model the receiver coil sensitivities using multi-channel (32 element) coil data. For validation, we use arbitrary data from a numerical phantom where the data satisfy the conventional MR signal equations. Using added noise of different magnitude and realizations, we show that the proton densities obtained have a bias close to zero and also low noise sensitivity. The obtained root-mean-square-error rate is less than 0.2% for the estimated proton density in a realistic 3D simulation. As an application, the method is used in a small cohort of MS patients, and proton density values for specific brain structures are determined.

Graphical abstract

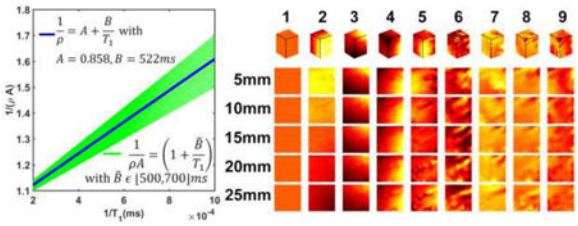

*Correspondence to: Dietmar Cordes, Ph.D., Cleveland Clinic Lou Ruvo Center for Brain Health, 888 W. Bonneville Ave, Las Vegas, NV, 89106, cordesd@ccf.org, Phone: 1-702-483-6022, Fax: 1-866-372-2720.

Keywords

quantitative MRI; proton density; T_1; transmission coil sensitivity; receiver coil sensitivity; bias field

1. Introduction

A difficult problem in quantitative MRI is the accurate determination of basic tissue parameters such as the longitudinal relaxation constant T_1 (Stikov et al., 2015) and the proton density ρ (Volz et al., 2012a), which are sensitive quantities in measuring brain tissue organization in a number of debilitating conditions such as multiple sclerosis (MS). Using Inversion Recovery (IR) sequences, T_1 can be estimated accurately (Stikov et al., 2015). The proton density, however, is more challenging to compute than T_1 because the transmit and receiver coil sensitivities need to be known as well. The RF transmission inhomogeneities need to be determined to correct for systematic errors in the B1 excitation field where tissue in the center of the brain experiences increased excitation (higher than the nominal flip angle) compared to tissue in the periphery (Wang et al., 2006). The RF receive field needs to be estimated because it is influenced by the individual subject-specific coil loading, the distance of the coil element from the tissue, and other intensity modulating effects such as eddy currents and nonlinearities of the gradient field. At 3T, the reciprocity theorem, due to standing wave and RF penetration effects, is no longer valid and the receiver coil sensitivity cannot be modeled as identical to the transmission coil sensitivity for a coil operating in both transmission and receive mode (Volz et al., 2012a). Thus, knowledge of the transmission sensitivity does not accurately describe the receiver coil sensitivity, but it can be approximated by a slowly spatially varying bias field and, via post-processing algorithms, can be approximately removed. However, different modeling of the bias field depending on the frequency content will lead to different values of the coil sensitivities and proton densities.

Individual receiver coil images (32 images for each coil element for a 32-channel coil) can also be collected and used to determine each coil sensitivity (Mezer et al., 2013). Another related approach uses a radial basis function expansion for modeling the receiver coil sensitivities and solving the proton density problem using the non-negative least squares optimization algorithm with multi-channel coil data (Cordes et al., 2015).

One promising method for estimating the bias field uses the inverse linear relationship between T_1 and ρ, as recently suggested (Abbas et al., 2014; Baudrexel et al., 2015; Mezer et al., 2016; Volz et al., 2012b). This relationship was derived from the fast exchange two-state model (Fatouras et al., 1991) and experimentally verified (Fatouras and Marmarou, 1999; Gelman et al., 2001).

Our study uses the same type of relationship in a more general framework by constructing 3D basis functions to model the receiver bias field. The novelty of this method is that the basis functions developed are suitable to cover an *entire range* of inverse linearities between T_1 and proton density. Rather than using this method in the entire brain or as was recently suggested to perform coil sensitivity estimation on small subsamples of the data (Baudrexel

et al., 2015), we partition the brain into small cubes. Using Principal Component Analysis (PCA), we obtain, in each cube, an optimal orthonormal set of basis functions derived from the data and a family of inverse linear T_1, ρ relationships, and model the receiver coil sensitivities using individual receiver coil information. Using a second partition of the brain with different cubes, we repeat the analysis. From the two different partitions, we derive linear algebraic equations without the need for using iterative optimization routines to determine the proton densities in the entire brain *simultaneously*, in *one* step, rendering the process more accurate and efficient.

We provide efficient and unbiased algorithms to solve this problem purely algebraically without any assumptions on the smoothness of estimated parameters or orders of approximation. For validation we use arbitrary data from a numerical phantom where the data satisfy the conventional signal equations for spoiled gradient (SPGR) and inversion recovery spin-echo echoplanar (IR-SE-EPI) data. Using added noise of different magnitude and realizations, we show that the proton densities obtained have a bias close to zero and low noise sensitivity. In addition to simulated data we also apply our method on publicly available sample data (raw data and analyzed data) of a healthy adult subject (Mezer et al., 2016). Finally, we compare our results with a recently published method by Mezer et al. (2016) and also with a bias correction method (Ashburner and Friston, 2005) that is available as a toolbox in SPM12 (Weiskopf et al., 2011).

We also apply our method to previously collected data in humans with multiple sclerosis (MS) (Mezer et al., 2013). Since this study is a proof- of-concept study introducing a novel algebraic analysis method and not a patient study, the MS data obtained should not provide a limitation in introducing our new method. The proposed method has been published as a proceeding at the annual ISMRM conference (Cordes et al., 2016).

2. Theory

Since the estimation of T_1 and observed transmission coil sensitivity m is not the main focus of this study, we refer to the Appendix where we have outlined the details of computing these quantities from the conventional signal equations for IR-SE-EPI data and SPGR data. We use the same notation of variables and follow similar overall steps as originally proposed in the study by Mezer et al. (2013). Fig.1 shows in the top portion a flow chart of the necessary steps involved for T_1 and m estimation. In the bottom portion of Fig.1, we provide another flow chart of the core contributions of this study, which we explain in more mathematical detail below. Even though our steps are similar to a previously published method, our algorithmic development contrasts strongly to the original study and recent study by Mezer et al. (2013, 2016), as will be explained in the Discussion section.

2.1 Receiver coil sensitivity

The signal amplitude M_0 is related to the receiver coil sensitivity g and proton density ρ by

$$M_0 = Cg\rho \quad (1)$$

where C is an arbitrary scaling constant related to the MR signal amplification factor. For a given $M_0(\vec{r})$ (where $\vec{r}$ is the position vector to a brain voxel q) and constant C, Eq.(1) contains two unknown functions $g(\vec{r})$ and $\rho(\vec{r})$. If these functions would have different frequency information (for example if $g(\vec{r})$ contains only low frequency components and $\rho(\vec{r})$ only high-frequency components), the solution of Eq.(1) would be trivial since both functions could be extracted from Eq.(1) by low and high frequency filters used on the logarithmic transform of Eq.(1). Such an approach is, however, not possible, because both functions have common frequency dependencies.

Using the SPGR sequence with a 32-channel head coil, we obtained for each channel individual coil images for the same signal amplification factor. In this case, the scaling constant C can be neglected. In the following, we set $C = 1$ and refer to ρ as the *unnormalized* proton density. For the i-th coil with signal $S^{(i)}$ and nominal flip angle α_n we obtain M_0 values, indexed by i, from the signal equation Eq.(A12) in the Appendix:

$$S^{(i)}(\alpha_n)=\frac{M_0^{(i)}(\alpha_n)\sin(m\alpha_n)(1-e^{-\frac{TR}{T_1}})}{1-\cos(m\alpha_n)e^{-\frac{TR}{T_1}}}. \quad (2a)$$

Then,

$$M_0^{(i)}(\alpha_n)=\frac{s^{(i)}(\alpha_n)(1-\cos(m\alpha_n)e^{-\frac{TR}{T_1}})}{\sin(m\alpha_n)(1-e^{-\frac{TR}{T_1}})}. \quad (2b)$$

To reduce measurement errors, we average over all four flip angles and obtain $\overline{M_0^{(i)}}=\mathrm{mean}_n M_0^{(i)}(\alpha_n)$ for voxel q at position $\vec{r}$. Then, proton density and i-th coil sensitivity need to be simultaneously estimated from

$$\overline{M_0^{(i)}}(q)=g^{(i)}(q)\rho(q). \quad (3)$$

2.2 Basis functions

Since the coil sensitivities are slowly varying functions, we partition the brain in non-overlapping cubes of size 30mm × 30mm × 30mm. Within each cube the coil sensitivities are modeled as a superposition of spatial basis functions $f_j(\vec{r})$, for $j = \{1, \ldots, J\}$, according to

$$g^{(i)}(\vec{r})=\sum_{j=1}^{J}A_j^{(i)}f_j(\vec{r}), \quad (4)$$

where the constants $A_j^{(i)}$ are unknown expansion coefficients for the *j*-th basis function corresponding to the *i*-th coil element.

2.3 Optimized basis functions

The relationship between T_1 and proton density ρ is given by

$$\frac{1}{\rho}=A+\frac{B}{T_1} \quad (5)$$

where A and B are constants which are slightly different for gray and white matter. At 3 Tesla, typical values are A = 0.879 and B = 503ms (Gelman et al., 2001) and A = 0.858 and B = 522ms (Volz et al., 2012b) for gray and white matter combined. Substituting Eq.(5) into Eq.(3), gives for the *i*-th coil sensitivity the expresion

$$g^{(i)}(\vec{r})=A\overline{M_0^{(i)}}(\vec{r})\left(1+\frac{\tilde{B}}{T_1(\vec{r})}\right)=\text{const.}\overline{M_0^{(i)}}(\vec{r})\left(1+\frac{\tilde{B}}{T_1(\vec{r})}\right) \quad (6)$$

where

$$\tilde{B}:=\frac{B}{A}. \quad (7)$$

Note that the *const.* term in Eq.(6) can be set to 1 because scaling and normalization of proton density is carried out separately in a later step. Since $\tilde{B}$ is of magnitude 572ms and 608ms (see above the values for A,B for the two references), we define a uniformly random variable $\tilde{B}$ in the interval [500, 700]ms and create a family of functions $g^{(i)}(\vec{r})$ from which we generate orthonormal basis functions $f_j(\vec{r})$ using principal component analysis (PCA). PCA diagonalizes the covariance matrix of the set of functions $g^{(i)}(\vec{r})$ and determines the corresponding eigenvalues and eigenvectors of the function space.

In the following we outline a practical algorithm to obtain the optimized spatial basis functions for a particular cube with Q voxels (for example $Q = 30^3 = 27000$). For $\tilde{B}$ we choose the values $\tilde{B}_l = 500ms + (l-1)10\ ms$, l = 1, …, 21. For the number of nearest coils we choose the value I, i.e. i = 1, …, I (for example I = 4). The functions that describe the coil sensitivities are then given by $g_l^{(i)}(\vec{r}) := \overline{M_0^{(i)}}(\vec{r})\left(1+\frac{\tilde{B}_\iota}{T_1(\vec{r})}\right)$. Next, we define the N × (I * 21) matrix X consisting of all coil sensitivity functions to be

$$X=[\ g_1^{(1)}(:),\ldots,g_{21}^{(1)}(:),g_1^{(2)}(:),\ldots,g_{21}^{(2)}(:),\quad\ldots\quad,g_1^{(I)}(:),\ldots,g_{21}^{(I)}(:)\ ]$$

$(:)=\begin{pmatrix}\vec{r}_1\\ \vdots\\ \vec{r}_Q\end{pmatrix}$ where indicates the position vectors of all voxels in the particular cube. We remove the column mean from X and solve the eigenvalue problem $X^TX\,V = V\Lambda$ where V and Λ are the eigenvector and eigenvalue matrices, respectively. If the eigenvectors are arranged so that the first eigenvector corresponds to the largest eigenvalue, the second eigenvector to the second largest eigenvalue, and so on, we choose the first n columns of the eigenvectors that explain at least 99.99% of the variance in matrix X. The optimized $n + 1$ basis functions for this cube are then given by the columns of the matrix $F=\left[\begin{pmatrix}1\\ \vdots\\ 1\end{pmatrix}, XV(:,1{:}n)\right]$, where we added as the first function a constant function.

PCA has been extensively used in classification, function approximation, and linear dimensionality reduction applications (Jolliffe, 2002). The PCA decomposition is done for each cube to obtain optimized orthogonal 3D basis functions that can represent a broad range of coil sensitivities and satisfy the inverse linear relationships (Eq.(5)) for an entire range of A and B values. Figure 2 illustrates the linear inverse relationship for our novel basis and the spatial appearance of the associated 3D basis functions for brain data of a typical cube in white matter.

2.4 Determination of the receiver coil sensitivities and proton densities

Using the compact notation $R_q := \frac{1}{\rho(q)}$, the equations to solve become

$$R_q^{(i)}=\frac{\sum_{j=1}^{J} f_{qj}A_j^{(i)}}{M_q^{(i)}} \quad (8)$$

where $M_q^{(i)} := \overline{M_0^{(i)}}(q)$ and $f_{qj} := f_j(\vec{r}(q))$ for all voxels $q = \{1, \ldots, Q\}$ that constitute each cube and $i = \{1, \ldots, I\}$ with $\max(I) = 32$ for a 32-channel head coil. We normalize the $M_q^{(i)}$ so that $\frac{1}{Q}\sum_{q=1}^{Q} M_q^{(i)}=1$ for all $i \in \{1, I\}$. A reasonable approach to find solutions of Eq.(8) is to minimize the variance of $R_q^{(i)}$ over the i-th coil estimates leading to the objective function

$$h_0=\frac{1}{2Q}\sum_{q=1}^{Q}\mathrm{var}_{p_i}\left(R_q^{(i)}\right). \quad (9)$$

The notation $\mathrm{var}_{p_i}(\cdot)$ means that the variance of the argument is taken with respect to the individual coils i so that each coil has a weight factor associated by the value p_i.

2.5 Equivalence to multimodal Canonical Correlation Analysis

We would like to point out that the solution for minimizing h_0 is equivalent to solving a multiset of equations arising in multimodal Canonical Correlation Analysis (mCCA) approaches. To see this equivalence, we can express Eq.(8) in vector notation with Q elements by

$$\overrightarrow{R}=F^{(i)}\overrightarrow{A}^{(i)} \quad (10)$$

where matrix $F^{(i)}$ is defined by

$$F^{(i)}=[\frac{f_{:,1}}{M_{:}^{(i)}},\ldots,\frac{f_{:,J}}{M_{:}^{(i)}}]. \quad (11)$$

An equivalent objective function to be minimized is then given by

$$h=\sum_{\substack{i\\ i\neq i'}}^{I}\sum_{i'}^{I}\|F^{(i)}\overrightarrow{A}^{(i)}-F^{(i')}\overrightarrow{A}^{(i')}\|^{2} \quad (12)$$

where the sum of terms within the norm symbol define a system of mCCA problems of the form

$$\mathrm{P}=\sum_{\substack{i\\ i\neq i'}}^{I}\sum_{i'}^{I}\mathrm{corr}(F^{(i)}\overrightarrow{A}^{(i)},F^{(i')}\overrightarrow{A}^{(i')}). \quad (13)$$

In this form the mCCA problem defines an eigenvalue CCA problem when $I = 2$. For $I > 2$ the mCCA problem is not an eigenvalue problem anymore and can only be solved iteratively (Kettenring, 1971; Li et al., 2009).

2.6 Algebraic Solution of the Proton Density Problem

We show that the minimization of h_0 (Eq.(9) can be obtained by purely linear algebraic (non-iterative) methods using matrix inversion without any optimization techniques that are based on gradient descent algorithms or methods that involve penalty parameters. This fact leads to a fast approach in solving the proton density problem. As shown in the Appendix, the solutions for minimizing h_0 satisfy the equations:

$$\sum_{i=1}^{I}\sum_{j=1}^{J}F_{lj}^{(m,i)}p_i(\delta_{m,i}-p_m)A_j^{(i)}=0 \text{ for } l=\{1,\ldots,J\}, m=\{1,\ldots,I\} \quad (14)$$

where $F_{lj}^{(m,i)}=\frac{1}{Q}\sum_{q=1}^{Q}\frac{1}{M_q^{(m)}M_q^{(i)}}f_{ql}f_{qj}$. Applying the transformations

$$t=J(i-1)+j \quad \text{and} \quad s=J(m-1)+l, \qquad (15)$$

Eq.(10) transforms to the system of equations

$$\sum_{t=1}^{I*J}\tilde{F}_{st}A_t=0, \qquad (16)$$

where $\tilde{F}_{st}=F_{jl}^{(i,m)}p_i(\delta_{m,i}-p_m)$, $A_t=A_j^{(i)}$ and $s=\{1,\ldots,I*J\}$. Since Eq.(16) is homogeneous, $\det(\tilde{F})=0$ due to linear dependencies of the equations for different s. Therefore, we can leave out one of the dependent equations and convert Eq.(16) into a nonhomogeneous system of equations by setting $A_1=1$. The minimum norm solution vector is then given by the generalized (Moore-Penrose) inverse (+) according to

$$\begin{pmatrix} A_2 \\ \vdots \\ A_{I*J} \end{pmatrix} = - \begin{pmatrix} \tilde{F}_{1,2} & \cdots & \tilde{F}_{1,I*J} \\ \vdots & \vdots & \vdots \\ \tilde{F}_{I*J-1,2} & \cdots & \tilde{F}_{I*J-1,I*J} \end{pmatrix}^{+} \begin{pmatrix} \tilde{F}_{1,1} \\ \vdots \\ \tilde{F}_{I*J-1,1} \end{pmatrix}. \qquad (17)$$

2.7 Simultaneous scaling of proton density values in all cubes

With Eqs. (17) and (4) we obtain the receiver coil sensitivities, and via Eq.(8) the *unscaled* proton densities ρ_k in each cube k for the selected partition of the brain into a set of cubes which we call set A. To scale the proton density for each cube so that the partition of all cubes have consistent proton density across the entire image, the proton density in each cube needs to be scaled by an unknown factor x_k, i.e. $\rho_k \rightarrow x_k\rho_k$. This scaling factor x_k is different for each cube k, because each cube was solved independently by Eq.(17). Note that this scaling step across all cubes does not normalize the proton density of CSF to 1 but provides only a proper scaling of all proton density values in the brain.

We repeat this rescaling process for a second partition of cubes (set B) that have been displaced to the first partition (set A) by one half of the cube length in all 3 dimensions. Then, the maximal intersection volume of a cube from set A and a cube from set B is equal to $\frac{1}{8}V$. The outcome of this process is that each voxel is a member of a cube $\in A$ and a member of a cube $\in B$, and has associated scaled proton densities $x_i^{(A)}\rho_i^{(A)}(q)$ for cube $i\in A$ and $x_j^{(B)}\rho_j^{(B)}(q)$ for cube $j\in B$, where $x_i^{(A)}$ and $x_j^{(B)}$ are the unknown scaling factors of each cube $i\in A$ and each cube $j\in B$, respectively. Since this is the same voxel, the proton densities must be the same in theory or equivalently, because of noise, the difference in

proton densities must be minimal. Then, the best scaling factors $x_i^{(A)}$ and $x_j^{(B)}$ can be determined so that the difference in proton densities for all voxels in the intersection volume of cube A and B is minimal.

In the following we provide a novel solution to this problem by simultaneously obtaining all scaling factors for all cubes in *one* step. This solution is achieved by minimizing the variance of the two estimates involving the same voxel in set A and B and integrating (summing) over all possible voxels: More formally using matrix notation, let $C_{qi}^{(A)}$ be the *unscaled* proton density of cube $i \in$ set A for voxel q. Similarly, let $C_{qj}^{(B)}$ be the *unscaled* proton density of cube $j \in$ set B for voxel q. Let the total number of cubes be I and J for set A and set B, respectively. We can then form the concatenated proton density matrix $C = [C^{(A)}\ C^{(B)}]$ with dimension of total number of voxels multiplied with the total number of cubes, i.e. $Q \times (I + J)$. This matrix has for each voxel q two nonzero column entries and thus is highly sparse. Since each cluster (i.e. column of matrix C) has an unknown scaling factor x_k, the scaled proton density matrix has the form

$$\tilde{C} = CX \quad (18)$$

where the X matrix is a diagonal matrix that contains the unknown scaling factors $\{x_1, \ldots, x_I, x_{I+1}, \ldots, x_{I+J}\}$ on the diagonal line. Note that $\{x_1, \ldots, x_I\}$ are the I scaling factors for all the I cubes of partition (set) A and similarly $\{x_{I+1}, \ldots, x_{I+J}\}$ are the J scaling factors for all the J cubes of partition B. A suitable objective function to be minimized is then given by

$$f(X) = \frac{1}{Q} \sum_{q=1}^{Q} \frac{1}{2} \mathrm{var}_k \tilde{C}_{qk}. \quad (19)$$

As shown in the Appendix, differentiation of this expression with respect to the diagonal components of X is similar to the problem in Eq.(9) and leads to the homogeneous matrix equation $Mx = 0$, where the components of M are given by

$$M_{lk} = \sum_{q=1}^{Q} C_{ql}(C_{ql}\delta_{kl} - \frac{1}{2} C_{qk}) \quad (20)$$

and $x = [x_1, \ldots, x_I, x_{I+1}, \ldots, x_{I+J}]^T$. Setting $x_1 = 1$ and defining

$$\tilde{M} = M_{1:I+J-1,2:I+J}, \quad (21.a)$$

$$\tilde{x}=[x_2,\ldots,x_I,x_{I+1},\ldots,x_{I+J}]^T, \quad (21.b)$$

$$y=M_{1:I+J-1,1}, \quad (21.c)$$

leads to the inhomogeneous matrix equation

$$\tilde{M}\tilde{x}=-y, \quad (22)$$

so that the solution vector is obtained by

$$\tilde{x}=-\tilde{M}^{-1}y. \quad (23)$$

2.8 Overall normalization to proton density of CSF

The final step of proton density normalization across the brain is by defining the proton density of CSF in the lateral ventricles to have the value $\rho = 1$. Since CSF is not uniform, it is common to use the mean value of ρ in the lateral ventricles for this normalization. However, the mean value of ρ in the ventricles may depend on the volume of the ventricles leading to small changes in the normalization. To arrive at a more reliable quantity, we use additional T_1 information and assign a proton density to be 1 for those voxels in CSF (obtained by SPM12 segmentation) that belong to the 98 percentile or larger in CSF proton density and have a T_1 value of 3700ms or larger. This value for T_1 is also consistent with Eq. (5) and yields $\rho = 1.0009$ for the given recent literature value of $A = 0.858$ and $B = 522$ms (Volz et al., 2012b).

3. Materials and Methods

3.1 Experimental Data

3.1.1 MR data acquisition—We used a limited data set made available from Mezer et al. (2013) containing 9 MS patients and 1 healthy control to demonstrate the novel algebraic approach to model the receiver coil sensitivities and determine the proton density. The acquisition protocol has been fully described in Mezer et al.(2013). Briefly the data were acquired on a GE scanner using 2D SE-IR EPI and 3D SPGR sequences with a 32-channel head coil. In particular, the SE-IR EPI sequence had a slab-inversion pulse and spatial-spectral fat suppression pulse. It was run with 4 different inversion times (TI 50ms, 400ms, 1200ms, 2400ms), TR 3s, resolution 1.9mm × 1.9mm × 4mm, TE minimum full (47ms), parallel imaging factor 2, same amplification settings, and the SPGR T1 sequence with 4 different flip angles (FA 4deg, 10deg, 20deg, 30deg, TR14ms, resolution 0.94mm × 0.94 mm × 1mm, TE 2ms, no parallel imaging). For the SPGR data, images were obtained for

each of the 32 channels. All data collected and obtained were in accordance with local IRB regulations. Total scanning time for these pulse sequences was about 22 min.

3.1.2 Preprocessing—All data were co-registered using affine transformation in SPM12 (http://www.fil.ion.ucl.ac.uk/spm/) to the 20deg 3D SPGR data. Segmentation was carried out in SPM12 using standard (default) parameters on the SPGR data. Masks for white matter, gray matter and CSF were combined to perform skull stripping. Possible distortions of the EPI data were significantly reduced using parallel imaging with factor 2, and no distortion correction was carried out.

3.1.3 Proton density estimation—For details of the steps involved in proton density estimation, we refer to the *Theory* section and the Appendix. A flow chart is given in Fig.1. Briefly voxel-specific T_1 values were calculated by minimizing Eq.(A4) from the SE-IR EPI images. Using the MR signal equation for the SPGR images with the known values for T_1, the observed transmission coil sensitivity was determined using Eqs.(A13-A14). After correcting the values of the flip angles in the signal equation for the SPGR, the signal amplitude $M_0^{(i)}$ was computed for each coil i (1 to 32) by Eq.(2). The receiver coil sensitivity and proton density have been simultaneously computed using Eq.(17) for different cubes and normalized using Eq.(23). Finally, an overall normalization of proton density to CSF and T_1 was carried out as described above. The only spatial filter used was applied for the estimated transmission and receiver coil sensitivities. In particular, to improve noise sensitivity for these two quantities, voxel-neighborhood averaging using the adjacent 26-voxels (or less voxels where the sensitivities are zero) was used.

3.2 Simulation

3.2.1 Toy Example in 2D—To show proof of concept of our method, we use a 3-coil two-dimensional toy example where we define the three coil receiver sensitivities on a 64×64 pixel grid to be a superposition of polynomial functions up to 2nd order and an additional slowly varying Gaussian function according to

$$\begin{pmatrix} g^{(1)}(x,y) \\ g^{(2)}(x,y) \\ g^{(3)}(x,y) \end{pmatrix} = 100 + \begin{pmatrix} 8.64 & 9.42 & 0.00097 & 0.00223 & 0.00746 \\ 7.81 & 2.53 & 0.00201 & 0.00835 & 0.00969 \\ 4.32 & 0.463 & 0.00539 & 0.0000934 & 0.00267 \end{pmatrix} \begin{pmatrix} x \\ y \\ x^2 \\ y^2 \\ xy \end{pmatrix} + 30G(x,y).$$

The Gaussian function $G(x,y)$ is defined by $G(x,y) = e^{-\frac{1}{2\sigma^2}[(x-32)^2+(y-32)^2]}$ with $\sigma = 40$. The logic behind these definitions is that we want to simulate coil sensitivities that are slowly varying but do not purely behave as low-order polynomial functions. This behavior is achieved by the addition of the Gaussian function that has a maximum in the center of the image at $x = y = 32$ and a large parameter σ. Note $G(32,32) = 1$ and $G(0,0) = 0.527$; thus the contribution of $G(x,y)$ to the coil sensitivities is almost unnoticeable by visual inspection of the image (see Fig.3, top row). The proton density $\rho(x,y)$ is simulated as a 64×64 uniform random image with values $0.5 < \rho(x,y) < 1$. Using Eq.(3), we calculate the corresponding

signal amplitudes $M_q^{(1,2,3)}$ with $q = (x,y)$ for each coil. We also compute a hypothetical $T_1(x,y)$ image that satisfies the inverse T_1,ρ relationship defined here by $\frac{1}{\rho}=0.879+\frac{503\text{ms}}{T_1}$. No noise is added for simplicity. The analysis compares 3 different methods used to estimate the coil sensitivities and proton density using Eq.(17). The first method uses as basis functions for $f_{qj} := f_j(x,y)$ the polynomial set of functions {*const*, *x*, *y*, *xy*, x^2, y^2}, which is identical with the polynomial set of functions of the ground truth. The second method uses an expanded set of polynomial functions up to 3rd order given by {*const*, *x*, *y*, *xy*, x^2, y^2, x^3, y^3}. The third method uses the proposed optimized basis functions as outlined in section 2.3. The obtained basis functions are similar to the ones in Fig. 2 except for the 2D case.

3.2.2 3D Brain Simulation—To show the accuracy of our method for a more realistic scenario, we carried out simulations using the ideal signal equations and generated pseudo SE-IR EPI and SPGR data. The SE-IR EPI data were simulated with 4 different inversion times (TI 50ms, 400ms, 1200ms, 2400ms), TR 3s and TE 47ms. The SPGR T1 data were simulated with 4 different flip angles (FA 4deg, 10deg, 20deg, 30deg), TR14ms and TE 2ms. Both the data were generated with a resolution 0.94mm × 0.94 mm × 1mm. For the SPGR data, images were simulated for each of the 32 channels. Specifically, for a given T_1 map and given maps for r_a and r_b obtained from real data (see Appendix (Eq.(A3)) for a definition of r_a and r_b), we calculated the signal map according to Eq.(A6) under the necessary condition that $(r_a+r_b e^{-\frac{TI}{T_1}})$ is monotonically increasing for increasing *TI*. Then, using an assumed transmission coil sensitivity m as well as receiver coil sensitivities $g^{(i)}$ obtained from maps of a different study, we created coil-specific SPGR images according to Eq.(8.a,b) by using $M_0^{(i)}=g^{(i)}\rho$ and by using the inverse linear relationship for ρ and T_1, i.e. $\frac{1}{\rho}=A+\frac{B}{T_1}$, according to Eq.(19) with A = 0.858 and B = 522ms. The transmission coil sensitivity used follows an approximate Gaussian distribution $m\sim N(1,0.16)$ where we limit the transmission coil sensitivity to be in the interval $m \in [0.4,1.6]$. To estimate the significance of a hypothetical deviation from this ideal equation, we investigated relationships up to second order according to the model $\frac{1}{\rho}=A+\frac{B}{T_1}+\frac{1}{2}\left(\frac{B}{T_1}\right)^2$. To use a realistic noise model for the simulation, we determined σ using the Rayleigh distribution of real data for regions outside of the brain with no signal for both SE-IR EPI and SPGR data (see Eq.(A2)), and then generated an approximate Gaussian distribution for regions with signal $S \gg \sigma$ that follow the model $y\sim N(\sqrt{S^2+\sigma^2},\sigma^2)$ (Gudbjartsson and Patz, 1995). Mean signal amplitude and noise for SE-IR EPI (TI=50ms) were $\bar{S}$ = 1063 and σ = 5.3, whereas for SPGR (FA=4deg) we determined $\bar{S}$ = 731 and σ = 41.5.

3.3 Comparison with other methods

Mezer et al. (2016) recently proposed a new method to estimate proton density using data collected with the same acquisition protocol as in Mezer et al. (2013). The proton density analysis is carried out using polynomial modeling of the receiver coil inhomogeneities together with an iterative optimization approach where the inverse linear relationship (Eq.5)

is being implemented as a penalty term. The penalty parameter is obtained using a cross validation approach. We performed three different comparisons. (a) Comparison of results using a 3D numerical brain phantom and (b) Comparison of results using real subject sample data (Mezer et al., 2016) and (c) Comparison of the CSF normalization step. We also compared our results for the 3D numerical brain phantom data and real subject sample data with results obtained using a bias correction method (Ashburner and Friston, 2005) that is available as a toolbox in SPM12 (Weiskopf et al., 2011).

4. Results

4.1 Toy Example in 2D

Figure 3 (top row, A) shows the simulated receiver coil sensitivities for coil 1 to 3 and proton density. Note that it is not possible to see the centered Gaussian function $G(x,y)$ contributing to the coil sensitivities because of the large $\sigma = 30$ used. Analysis using the same polynomial basis set as in the ground truth setup shows a small error in the obtained coil sensitivities and proton density with mean($|\Delta\rho(x,y)|$) =1.18% and max($|\Delta\rho(x,y)|$) = 4.7% (see Fig.3 2nd top row, B). If the number of basis functions is increased to include two more polynomial functions of 3rd order, the error increases significantly for all coil sensitivities and proton density (see Fig.3, 3rd top row, C). Specifically, we obtain error rates of mean($|\Delta\rho(x,y)|$) = 5.0% and max($|\Delta\rho(x,y)|$) = 12.8%. Using the proposed optimized basis functions (see Fig.3, last row, D), we obtain a very low error rate with mean($|\Delta\rho(x,y)|$) = 0.93% and max($|\Delta\rho(x,y)|$) = 2.0%.

4.2 3D Brain Simulation

Figure 4 shows images of the ground truth of the simulated data and estimated parameters (T_1, observed transmission coil sensitivity m, receiver coil sensitivity g, proton density ρ) using the methods described before. The structure of the basis functions obtained are similar to Fig. 2 because we used numerical phantom data derived from actual human subject data. For most voxels, only the first 4 basis functions contribute significantly. However, to obtain minimum error rate we used 41 functions for each cube. Minor differences between ground truth and estimated parameters can be seen for the observed transmission coil sensitivity and receiver coil sensitivity.

A more quantitative comparison is shown as scatter plots in Fig.5. T_1-estimation shows that the error slightly increases with the magnitude of T_1 up to 3000ms. Similarly, the error in the estimation of the observed transmission coil sensitivity increases with the magnitude of m. The receiver coil sensitivity has a more constant error behavior across the range of g. The proton density has a very small error rate which is nearly constant for values of $\rho > 0.7$.

An overall comparison of the error rate as a function of noise level is provided in Fig.6. It is shown that T_1 estimation has a root-mean-squared error (RMSE) of 0.4%, observed transmission coil sensitivity 0.8%, receiver coil sensitivity 0.7%, and proton density <0.2%. The noise sensitivity of the estimated proton density is by a factor of about 2 smaller than the noise sensitivity of the estimated T_1 values because the chosen basis functions incorporate the inverse linear relationship between T_1 and proton density (Eq.(5)). Even if

the data were generated using constants $A = 0.858$, $B = 422$ms giving $\tilde{B} = 492$ms, which are not part of the optimized basis functions interval for $[\tilde{B}] \in [500,700]$ms, the RMSE for the proton density increases only to 1.2%. Finally, using a hypothetical quadratic model according to $\frac{1}{\rho} = A + \frac{B}{T_1} + \frac{1}{2}\left(\frac{B}{T_1}\right)^2$ as described above, the RMSE for the proton density increases to 2.0%. Table 1 summarizes these findings.

4.3 Comparison with a recently published method by Mezer et al. (2016)

4.3.1 Comparison using the 3D numerical brain phantom—In the first comparison (Fig.7), we analyzed simulated data from our 3D numerical brain phantom using the publicly available code by Mezer et al. (2016) with default options. Fig.7A shows 3 slices of the proton density ground truth. Fig.7B shows the results obtained according to Mezer et al. (2016) We rescaled the images in Fig.7B so that the mean value for the proton density is the same as in the ground truth images to avoid overall scaling differences that arise from the last step where the proton density is normalized to CSF in the ventricles (see section "*Overall normalization to proton density of CSF*"), because this normalization step is usually implemented slightly different by different authors. Fig.7C shows the difference map for ρ(Mezer et al) – ρ(ground truth) in percent. The RMSE error and median error are 3.7% and 2.0%, respectively. For comparison with our method we show in Fig.7D the difference map for ρ(this research) – ρ(ground truth). Here, the RMSE and median error are 0.13% and 0.08%, respectively.

Of particular interest is the bias obtained for estimation of ρ in gray matter and white matter for our method. To reduce partial volume effects involving CSF, we created 95 percentile masks of gray matter and white matter. We obtained a median difference of ρ(our method) – ρ(ground truth) in gray matter and white matter to be -0.0064% (RMSE 0.08%) and -0.11% (RMSE 0.14%), respectively. Thus, the estimation of gray matter is practically unbiased (very close to zero) and white matter is slightly underestimated by our method.

4.3.2 Comparison using real subject data—Fig.8A shows the scaled proton density results for 3 slices according to Mezer. Fig.8B shows the results obtained according to our method. To facilitate better comparison, the images in A were scaled so that the mean proton density is the same for A and B. The re-scaling avoids any bias according to the different normalization step chosen by the authors to adjust for proton density values of CSF. Fig.8C shows the difference map for ρ(Mezer et al., 2016) – ρ(this research) in percent. The RMSE difference and median difference are 5.0% and 2.6%, respectively. For this comparison we created a mask from the images in B and eroded from the border in B voxels in a cube with edge length of 3 voxels so that border and registration effects are negligible. This mask was then applied to the images in A.

4.3.3 Comparison of the CSF normalization step—Mezer et al. (2016) chooses for the overall CSF normalization step voxels in the central portion of the lateral ventricles so that $\rho = 1$ for $T_1 = 4.3s$. Our approach to normalization is slightly different (see section "*Overall normalization to proton density of CSF*"). To show this difference between both methods, we calculated the empirical cumulative density distribution of the proton density

values in the lateral ventricles. Fig.8D shows the results obtained. Note that our method does not have proton density values larger than 1 within the lateral ventricles whereas with the method by Mezer et al. (2016), 20% of voxels in the lateral ventricles have values larger than 1. Due to the different normalization step, the mean (and median) proton densities in gray matter and white matter are also different by about 3% to 4%. According to the method of Mezer et al. (2016) ρ(GM) = 0.845 ± 0.046, median ρ(GM) = 0.845, ρ(WM) = 0.740 ± 0.055, median ρ(WM) = 0.725, whereas with the proposed method (this study) we obtain ρ(GM) = 0.809 ± 0.052, median ρ(GM) = 0.806, ρ(WM) = 0.712 ± 0.052, median ρ(WM) = 0.702.

4.4 Comparison with a standard bias field correction method

Table 2 shows results using a standard bias field correction method as implemented in SPM12. This method was used as a standard comparison in a previous publication; however, the authors only used default parameters (Volz et al., 2012b). We applied this method to the same simulated data used before where $\frac{1}{\rho}=0.858+\frac{522\text{ms}}{T_1}$ and $\tilde{B}$ = 608*ms*. The M_0 map was treated as a structural image and segmented with the toolbox in SPM12 (Ashburner and Friston, 2005). Rather than using default parameters (FWHM 60mm, regularization 0.001), we performed segmentations over the 2D grid parameter space with FWHM ∈ [40, 50, …, 130] mm and regularization ∈ [0, 10^{-5}, 10^{-4}, 10^{-3}, 10^{-2}] to find the best combination of parameters. The obtained bias field was inverted to obtain the combined coil sensitivity map *g*. Then, using Eq.(1), the unnormalized proton density map was obtained and normalized to CSF in the ventricles, as outlined before. Values of the proton density and corresponding RMSE were computed. A search over the entire parameter space gave a minimum error of 4.1% relative to the ground truth for the proton density. It is obvious that such a grid search cannot be performed when the ground truth is unknown, and from our simulation it is expected that the relative error of the proton density is about 4% or larger.

4.5 Effect of Grid size

With a grid size of 30mm, we parcellated the brain into cubes containing 30^3 voxels We found this parcellation size to be optimal in terms of anatomical coverage of all slices and computational efficiency. We re-ran our analysis with other sizes such as 10mm, 15mm, 20mm, 25mm, 30mm, 35mm and 40mm and did not find differences in terms of the final accuracy for the proton density. With 35 and 40mm sizes, the last slice could not be covered fully.

4.6 Accuracy as a function of the number of coils

We also ran the proton density estimation as a function of the number of nearest coils included to the cube in question. Using only the 2 nearest coils gave good results, and using more than 4 nearest coils did not provide any advantages in terms of accuracy. We thus used for each cube the 4 nearest coils in the estimation of the proton density. For the toy example in 2D, excellent results with a maximum error less than 2% could be achieved with 3 coils but not with 2 coils. For a single coil element, the proton density problem is not solvable with high accuracy. However, combining multiple coil elements (or all 32 coil elements) into

a single image which can then be used for proton density estimation is promising (Mezer et al., 2016).

In Eq.(9), it is possible to assign different weight factors p_i for each coil. The notion for using different weight factors is that whether the i-th coil is close or further away, a different value for p_i may be used to obtain optimal results. To determine optimum weight factors, we used a Broyden-Fletcher-Goldfarb-Shanno (BFGS) algorithm (see for example Nocedal and Wright, 1999). Interestingly, once $M_q^{(i)}$ in Eq.(9) was normalized to a mean of 1 for all coils, the optimal weight factors were found to be $p_i = 1$ (or very close to 1) for all coils.

4.7 Real data

Figure 9 shows results obtained for a representative subject (subject #1). We calculated T_1 maps and estimated the transmission coil sensitivity m. Then, we estimated the SPGR signal amplitude M_0 using Eq.(1), and calculated receiver coil sensitivity maps and proton density maps. This proton density is normalized as calculated by Eq.(23). A final overall normalization was obtained using information from CSF and T_1. Table 4 lists estimated A and B values for all subjects in gray matter, lesion-free white matter, whole brain, and MS lesions. Table 5 lists individual T_1 and ρ values in selected regions of the brain, i.e. in gray matter, lesion-free white matter, MS lesion, left and right caudate and left and right putamen. Finally, Table 6 shows a comparison of obtained proton density results with values from literature.

5. Discussion

5.1 Novel 3D basis set

The purpose of this research project was to simultaneously estimate the receiver coil sensitivity and the proton density using data from individual multi-channel coil images. We developed a novel basis set that can represent with high accuracy the receiver coil sensitivities of the individual coil images. Rather than relying on a fixed value of parameters A and B of the inverse linear relationship between T_1 and ρ (Eq.5), our basis set includes an entire interval of {A, B} parameters and is data-driven because we determine the coils sensitivities from the data itself (using M_0) and weight the sensitivities by a family of functions that satisfy the inverse T_1, ρ relationship over a large parameter space. We then use PCA to obtain a compact orthonormal 3D basis functions set for each cube and retain the most significant basis functions. The compact orthonormalization step leads to excellent stability in solving the linear equations.

5.2 Comparison to other basis sets

If uninformed (no relationship to Eq.(5)) basis functions are used, such as polynomial functions up to second or third order, we could not obtain an accurate estimate of the receiver coil sensitivities and proton densities for the 3D case using algebraic solutions. We have shown that this behavior also occurs for a 2D toy example where we simulated coil sensitivities as a superposition of polynomial functions up to 2nd order and a Gaussian function. When the basis set matched the basis of the coil sensitivities, the modeled subspace is optimal and gives a very low error rate in the estimation of coil sensitivities and proton

density. However, when the basis is extended to include higher order terms which do not match the ground truth in modeling of the coil sensitivities, the error rate increases. On the other hand, using our optimized basis function approach for the modeling of the coil sensitivities, the obtained error for the estimated coil sensitivities and proton density is very low due to better modeling of the subspace of coil sensitivities with the additional T_1 information. Furthermore, if simulations are designed with coil sensitivities that can be perfectly described by second or third order functions, then a second or third order polynomial basis set will provide exact solutions. For the more realistic 3D brain simulation, we could not obtain a RMSE of the proton density less than 10% using polynomial basis functions up to third order, as described in the results section.

For our brain simulation, we used actual receiver coil sensitivities of individual coils obtained from a previous bias estimation procedure using SPM12. The bias field cannot be described accurately by a combination of low-order polynomials. We also experimented with radial basis functions of the form $f_j^{(i)}(\vec{r}) = e^{-\frac{\left|\vec{r}-\vec{r}_j^{(i)}\right|^2}{2\sigma^2}}$ with center $\vec{r}_j^{(i)}$ and parameter σ for each coil i. By including up to 200 radial basis function for each cube, we could not get a RMSE of ρ with less than 8%.

5.3 Combination of different basis sets

We also tried basis functions using low-order polynomial functions in combination with the optimal 3D basis functions as described in the Methods section. Improvements were marginal. In addition, instabilities arose in a few of the 100 cubes when mixed basis sets were used and proper expansion coefficients could not be determined even after orthonormalization of the combined basis. Similar results were obtained when we tried basis functions consisting of second order polynomials in combination with radial basis functions.

5.4 Error sensitivity

With our method we obtained a high accuracy in proton density using a realistic 3D simulation with RMSE less than 0.2%. From Eq. (5) it follows by differentiation that the relative noise sensitivity of the proton density is always smaller than the relative noise sensitivity of T_1 since it can be shown that

$$\frac{\Delta\rho}{\rho} = \frac{\rho B}{T_1}\frac{\Delta T_1}{T_1} < \frac{\Delta T_1}{T_1} \quad (24)$$

where the term $\frac{\rho B}{T_1}$ is about 0.3 for brain tissue. Since the basis functions needed to model the individual coil images are unknown, the use of Eq.(5) provides a method to generate optimized basis functions with low noise sensitivity according to Eq.(6). Thus, there is no noise amplification using our new method because Eq.(5) acts as a form of constraint for the estimated proton density values with low error sensitivity. This fact explains the almost constant error sensitivity of the estimated proton density.

5.5 Real data

For real data, we found A and B values concordant with literature. We also determined values for A and B for gray matter, lesion-free white matter and MS lesions. We found small deviations in the parameters for lesions and lesion-free white matter. Thus, lesion detection may benefit from using the difference in estimated values for A and B. For all subject data analyzed, we found that all determined $\tilde{B}$ values were in the interior region of the assumed interval range as proposed according to Fig.2.

5.6 Fine structure of the estimated transmission sensitivity

We would like to make the distinction that in this study, we have only estimated the *observed* but not the *usually-defined* transmission sensitivity because we estimate all quantities from actual brain data. Usually, it is expected to obtain a true low-frequency spatially smooth transmission sensitivity when homogeneous phantoms are used. In our case using only subject data, the observed transmission sensitivity has some fine structure which may indicate an incomplete model for the signal equation used in the estimation process. There also could be potential magnetic interactions from different tissue compartments which will not produce a low frequency spatially smooth transmission sensitivity. Furthermore, using simulated data of arbitrary nature (whether spatially smooth or not), we have shown that the transmission sensitivity is the most difficult parameter to compute and has the largest error rate (0.9%) among all estimated parameters. Some of these deficiencies can be attributed to the fact that we neglected T2* effects and incomplete spoiling effects of the transverse magnetization by the SPGR sequence (see for example Preibisch and Deichmann, 2009). A potential modification to obtain smoother maps would be by using a spatial Gaussian smoothing kernel on the observed transmission sensitivity. We have refrained from such an ad-hoc solution (except the immediate-neighboring-voxel-averaging as mentioned before in section *Data analysis*) because the required smoothing kernel is unknown and cannot be estimated from the obtained subject data. However, we have carried out simulations where we incorporated Gaussian spatial smoothing with different FWHMs in the estimation process but were not successful to lower the error rate for more spatially extended FWHM >1cm.

5.7 Comparison to the study by Mezer et al. (2016)

The method by Mezer et al. (2016) uses low-order polynomial functions that acts as smoothness constraints to model the receiver coil sensitivities. Polynomial functions have been proposed before for this purpose (see for example Baudrexel et al., 2015, Mezer et al., 2013; Volz et al., 2012). After determining T_1 and estimating the true flip angle using nonlinear least square optimization, the proton density problem is formulated as an iterative least square optimization problem that uses the inverse T_1, ρ relationship as an additional penalty term with unknown penalty parameter strength λ. The penalty parameter strength is then determined in a secondary step using a cross-validation approach. The penalty term acts as a regularization of the proton density by penalizing deviations from the inverse T_1, ρ relationship. Also, the code available does not use multi-channel coil data since it is stated that the combined single channel coil data leads to equivalent results.

Our approach to model the receiver coil sensitivities is very different. We propose a novel algebraic approach that does not involve regularizations, low-order polynomial fittings, penalty terms, cross validations and iterative optimizations. We also emphasize that modeling of the receiver coil sensitivities can be directly derived from the data and a family of inverse linear T_1,ρ relationship by PCA. Using the dominant PCA components, the basis functions are automatically orthonormal and satisfy the inverse T_1,ρ relationship over an entire interval rather than using a specific value for this relationship. To solve the proton density problem, we use standard matrix inversion routines only, and the advantage of a purely algebraic method is improved speed and accuracy. Since our method is purely algebraic, it is fast and accurate. Using multi-coil data, our simulation showed that polynomial functions may lead to unstable solutions of the proton density estimation problem whereas instabilities do not arise with our proposed PCA method.

We also would like to point out the different registration methods. Mezer et al. (2016) uses ANTs (http://stnava.github.io/ANTs/), whereas we use standard SPM12 functions for registration. The use of different registration techniques may lead to differences in intensity borders and a different smoothness due to different interpolation strategies. In our comparison (see Results section), the outer borders are truly effected, when comparing the same data with different registration methods. To exclude border effects in the comparison, we calculated the median proton density value which is a more robust quantity. Our results on simulated data showed better agreement to the ground truth than the method by Mezer et al. (2016).

We obtained a practically unbiased proton density estimation in gray matter and a very small bias in white matter. The slightly underestimated proton density in white matter (bias = -0.11 %) may be explained by the fact that it is more difficult to determine the transmission coil sensitivity in the interior region of the brain that constitutes mostly CSF plus white matter than in the region near the outer boundary that constitutes most of the cortical gray matter. In Fig.4B, the transmission coil sensitivity is on average larger in white matter than in gray matter. Fig.5B shows that for all quantities determined, the uncertainty in determining the transmission coil sensitivity is largest for large values of the transmission coil sensitivity ($m > 1$ in Fig.5B). Since values for $m > 1$ occur on average more frequently in white matter, we obtain a larger uncertainty in estimating the proton density in white matter. This also explains the slightly larger RMSE obtained for white matter than for gray matter. However, the bias obtained is very small when compared to other methods and could also be partially due to differences in the noise realizations together with partial volume errors introduced by coregistration of all generated images using SPM12.

For real subject data, we obtain proton density values that are 3% to 4% less compared to the results of Mezer et al. (2016). However, due to different overall normalization strategies, small differences in results are to be expected.

5.8 Comparison with a standard bias-field correction method

The standard bias-field correction method implemented in SPM was used previously by Volz et al. (2012) for modeling of the receiver coil sensitivities using default parameters (FWHM=60mm, regularization=0.001). With default parameters, we obtain a fairly large

error (RMSE=6.6%) in proton density estimation using our numerical phantom. Even after numerical optimization of the parameters, we were not able to obtain an error less than 4.1%. For real data, the optimal parameters of the bias correction method are still unknown because of the missing ground truth.

For our MS data another potential concern is that larger lesions may change the estimation of the bias-field which could alter the value of the proton density at and near lesions. With our method, however, it is more conceivable that the coil sensitivities are better modeled because of the data-driven nature and inclusion of the larger subspace using a family of inverse T_1, ρ relationships. Furthermore, as pointed out by Volz et al. (2012), anatomical variability such as increased CSF spaces due to enlarged ventricles may lead to an increased error in proton density using the standard bias-field correction method. Our proposed method does not depend on anatomical variability.

5.9 Future potential studies and shortcomings of the current methodology

Regarding pathologies where, for example, local deposits of iron leads to shortening of T_1, the inverse linear relationship between T_1 and ρ is invalid and it may be more suitable to add basis functions to the optimized set that approximately describes this relationship. However, more detailed studies of this nature addressing pathologies with T_1 shortening are beyond the scope of this research project.

5.10 Computational considerations

All calculations were performed in MATLAB (The Mathworks, Inc., version R2015b) on a Dell-workstation with Intel Xeon E5-2687W architecture running at a clock speed of 3.4GHz and equipped with 96GB of memory. We employed vectorization for the T_1 grid and parallelization with 8 workers for the T_1 estimations of all voxels. The time necessary to determine T_1 and observed transmission coil sensitivity m was 4.8 min, for receiver coil sensitivity g and unscaled proton density ρ estimation 7.3 min and for proton density ρ scaling and normalization 2.5 min. The entire process after coregistration and segmentation by SPM12 from start to finish took 15 min for one subject.

5.11 Clinical applications

The novel method introduced for quantitative measurement of the proton density is not limited to using the 32-channel head coil with axial acquisitions. It will work for any surface coil device where multi-channel data can be acquired in any spatial geometry. Potential clinical applications involve quantitative water content mapping in multiple sclerosis to determine demyelination tissue properties of white and gray matter lesions (Laule et al., 2004, 2006; Mezer et al., 2013). Other applications include quantitative imaging of edema that frequently arise in head trauma, stroke, brain tumors and other brain diseases such as hepatic encephalopathy (Ajata and Robber, 2002, Andersen, 1997; Neeb and Shah, 2006; Neeb et al., 2006; Oros-Peusquens et al., 2014; Shah et al., 2003, 2008).

6. Conclusions

We proposed a new algorithm to more accurately model the receiver coil sensitivities to produce nearly unbiased proton density maps with low noise sensitivity. Using optimized basis functions for the modeling of the individual receiver coil sensitivities allows an accurate estimation of inhomogeneities of the signal due to receiver coil bias. The final images of the computed proton densities and individual receiver coil sensitivities are solutions of the MR signal equations. Our method is particularly suitable for quantitative diagnostic assessment of brain tissue because of its low bias and low noise sensitivity.

Acknowledgments

This research project was supported partially by the NIH (COBRE grant 1P20GM109025) and 1R01EB014284. The authors would like to thank A. Mezer for helpful discussions, sharing of data and software in the initial stages (Fall 2014) of this research project.

Appendix A

A.1 T_1 estimation

We follow the approach as originally suggested by Barral et al. (2010) with some minor modifications. Due to collection of magnitude MR data, the noise in the MR images has a Rician distribution. We reduce the bias associated with magnitude images by calculating an adjusted magnitude amplitude S given by

$$S = \sqrt{|M^2 - \sigma^2|} \quad \text{(A1)}$$

where M is the magnitude image value (Gudbjartsson and Patz, 1995). The noise σ is estimated from the Raleigh distribution of the noise in an image region where there is no NMR signal using the relationship

$$\overline{M}_{\text{air}} = \sigma \sqrt{\frac{\pi}{2}} \quad \text{(A2)}$$

where $\bar{M}_{air}$ is the mean signal in an image region outside the brain.

The signal equation for magnitude IR data has the form

$$S(TI_n) = \left| r_a + r_b e^{-\frac{TI_n}{T_1}} \right| \quad \text{(A3)}$$

where r_a and r_b are functions of M_0, TR, T_1, TE, θ_1, θ_2, θ_3 for a SE-IR $(\theta_1 - TI - \theta_2 - \frac{TE}{2} - \theta_3 - TR - TI - \frac{TE}{2})$ sequence under the usual assumptions that the RF pulses are instantaneous, the spoiling of M_{xy} after each echo acquisition is perfect and there are no off-resonance effects. The term TI_n in Eq.(A3) labels the different inversion times and T_1 is the unknown longitudinal relaxation time. There are no other approximations done and Eq.(A3) is valid for any TR, T_1 and T_2 [Barral et al., 2010]. Using least-square minimization with polarity restoration (12) gives the objective function

$$J_\tau = \sum_{n=1}^{N} \left[\gamma_\tau(TI_n) y(TI_n) - (r_a + r_b e^{-\frac{TI_n}{T_1}})\right]^2, \quad \text{(A4)}$$

where n counts the number of different inversion times TI_n (in our case $N = 4$),

$$\gamma_\tau(TI_n) = \left\{ \begin{array}{ll} 1 & \text{if } TI_n \geq \tau \\ -1 & \text{if } TI_n < \tau \end{array} \right\} \quad \text{(A5)}$$

is the polarity restauration function, $y(TI_n)$ is the magnitude signal corresponding to inversion time TI_n, and τ is the zero-crossing point of Eq.(A5). Since the function $f(TI) = (r_a + r_b e^{-\frac{TI}{T_1}})$ is monotonically increasing for $r_b < 0$ (Barral et al., 2010), i.e.

$$\frac{d}{dTI}(r_a + r_b e^{-\frac{TI}{T_1}}) = r_b e^{-\frac{TI}{T_1}}(\frac{-1}{T_1}) > 0 \quad \text{(A6)}$$

there are only 5 possibilities for $\gamma_\tau(TI_n)$ given $TI_1 < TI_2 < TI_3 < TI_4$. These are

$$(\gamma_\tau(TI_1), \gamma_\tau(TI_2), \gamma_\tau(TI_3), \gamma_\tau(TI_4)) = \left\{ \begin{array}{ll} (1,1,1,1) & \text{if } S(TI_1) \text{ is minimum} \\ (-1,1,1,1) & \text{if } S(TI_1) \text{ or } S(TI_2) \text{ is minimum} \\ (-1,-1,1,1) & \text{if } S(TI_2) \text{ or } S(TI_3) \text{ is minimum} \\ (-1,-1,-1,1) & \text{if } S(TI_3) \text{ or } S(TI_4) \text{ is minimum} \\ (-1,-1,-1,-1) & \text{if } S(TI_4) \text{ is minimum} \end{array} \right\}. \quad \text{(A7)}$$

Partial differentiation with respect to the unknowns in Eq.(A4) and substitution results in a 1-dimensional equation for T_1 which can be solved over a grid for $T_1 \in [1,5000]$ms with spacing 1ms for the scenarios in Eq.(A7). The solution is obtained for the T_1 that minimizes Eq.(A4). Using the notation

$$A=\sum_n \gamma_\tau y \quad \text{(A8.a)}$$

$$B=\sum_n \gamma_\tau y e^{-\frac{TI_n}{T_1}} \quad \text{(A8.b)}$$

$$C=\sum_n \gamma_\tau y TI_n e^{-\frac{TI_n}{T_1}} \quad \text{(A8.C)}$$

$$D=\sum_n e^{-2\frac{TI_n}{T_1}} \quad \text{(A8.d)}$$

$$E=\sum_n e^{-\frac{TI_n}{T_1}} \quad \text{(A8.e)}$$

$$F=\sum_n TI_n e^{-\frac{TI_n}{T_1}} \quad \text{(A8.f)}$$

$$G=\sum_n TI_n e^{-2\frac{TI_n}{T_1}}, \quad \text{(A8.g)}$$

the partial derivatives of the objective function become:

$$\frac{\partial}{\partial r_a} J_\tau = -A + r_a N + r_b E \quad \text{(A9.a)}$$

$$\frac{\partial}{\partial r_b} J_\tau = -B + r_a E + r_b D \quad \text{(A9.b)}$$

$$\frac{\partial}{\partial T_1} J_\tau = -r_b C + r_a r_b F + r_b^2 G. \quad \text{(A9.c)}$$

At the minimum of J_τ all derivatives must vanish. Then, r_a and r_b can be isolated from Eqs. (A2a,b) resulting in

$$r_a = \frac{AD - BE}{ND - E^2} \quad \text{(A10.a)}$$

$$r_b = \frac{NB - AE}{ND - E^2}. \quad \text{(A10.b)}$$

The value for T_1 is estimated by substituting Eq.(A3a) and Eq.(A3b) in the objective function J_τ (see Eq.(A4)) and searching for the minimum value of J_τ over all T_1. This method is fast because the grid search can be vectorized.

A.2 Observed transmission coil sensitivity

The true flip angle α is related to the nominal flip angle α_n that is prescribed at the scanner console by

$$\alpha = m\alpha_n \quad \text{(A11)}$$

where m is called the observed transmission coil sensitivity. We estimate m from obtained SPGR images in steady states with four different flip angles using combined 32-channel image data. Using Eq.(A11), the SPGR signal equation is given by

$$S(\alpha_n) = \frac{M_0 \sin(m\alpha_n)(1 - e^{-\frac{TR}{T_1}})}{1 - \cos(m\alpha_n)e^{-\frac{TR}{T_1}}} \quad \text{(A12)}$$

where TR is the repetition time and M_0 a constant that is proportional to the proton density and the receiver coil sensitivity. In Eq.(A12) we have neglected the T2* decay factor $e^{-\frac{TE}{T_2^*}}$ because our echo time is small (2ms). We determine the two unknowns (M_0, m) by a novel approach based on least square minimization over all four flip angles, i.e.

$$\min_{m,M_0} \sum_{n=1}^{4} \left(S(\alpha_n) - \frac{M_0 \sin(m\alpha_n)\left(1 - e^{-\frac{TR}{T_1}}\right)}{1 - \cos(m\alpha_n)e^{-\frac{TR}{T_1}}} \right)^2. \quad \text{(A13)}$$

Since M_0 is a scaling factor, partial differentiation of Eq.(A13) with respect to M_0 and setting the result to zero leads to

$$M_0=\frac{\sum_{n=1}^{4}S(\alpha_n)\sin(m\alpha_n)(1-\cos(m\alpha_n)e^{-\frac{TR}{T_1}})^{-1}}{\sum_{n=1}^{4}\sin^2(m\alpha_n)(1-e^{-\frac{TR}{T_1}})(1-\cos(m\alpha_n)e^{-\frac{TR}{T_1}})^{-2}}. \quad \text{(A14)}$$

We can now substitute M_0 in Eq. (A13) and obtain a 1-dim minimization problem for the unknown m which we solve efficiently by a vectorized grid search using all $m \in [0,2]$ with step size 0.001. After the solution for m is obtained, we use Eq.(A14) and compute M_0. Our approach provides the global minimum with respect to the variables m and M_0. This approach to determine M_0 (Eq. (A14)) has not been published before to the best of our knowledge.

A.3 Proton density estimation

The objective function is given by Eq.(9), i.e.

$$h_0=\frac{1}{2Q}\sum_{q=1}^{Q}\underset{p_i}{\text{var}}\frac{\sum_{j=1}^{J}f_{qj}A_j^{(i)}}{M_q^{(i)}}. \quad \text{(A15)}$$

Using the relationship

$$\text{var}(v)=E(v^2)-E^2(v), \quad \text{(A16)}$$

where E labels the expectation value and v is some random variable, we obtain

$$\begin{aligned}
h_0&=\tfrac{1}{2Q}\textstyle\sum_{q=1}^{Q}\left(\sum_{i=1}^{I}p_i\left(\frac{\sum_{j=1}^{J}f_{qj}A_j^{(i)}}{M_q^{(i)}}\right)^2-\left(\sum_{i=1}^{I}p_i\left(\frac{\sum_{j=1}^{J}f_{qj}A_j^{(i)}}{M_q^{(i)}}\right)\right)^2\right)\\
&=\tfrac{1}{2Q}\textstyle\sum_{q=1}^{Q}\left(\sum_{i=1}^{I}p_i\sum_{j=1}^{J}\sum_{j'=1}^{J}\frac{f_{qj}A_j^{(i)}}{M_q^{(i)}}\frac{f_{qj'}A_{j'}^{(i)}}{M_q^{(i)}}-\sum_{i=1}^{I}p_i\sum_{i'=1}^{I}p_{i'}\frac{\sum_{j=1}^{J}f_{qj}A_j^{(i)}}{M_q^{(i)}}\frac{\sum_{j=1}^{J}f_{qj}A_j^{(i')}}{M_q^{(i')}}\right)\\
&=\tfrac{1}{2}\textstyle\sum_{i=1}^{I}\sum_{i'=1}^{I}\sum_{j=1}^{J}\sum_{j'=1}^{J}\frac{1}{Q}\sum_{q=1}^{Q}\frac{f_{qj}f_{qj'}}{M_q^{(i)}M_q^{(i')}}(p_i\delta_{i,i'}-p_ip_{i'})A_j^{(i)}A_{j'}^{(i')}\\
&=\tfrac{1}{2}\textstyle\sum_{i=1}^{I}\sum_{i'=1}^{I}\sum_{j=1}^{J}\sum_{j'=1}^{J}F_{jj'}^{(i,i')}p_i(\delta_{i,i'}-p_{i'})A_j^{(i)}A_{j'}^{(i')}
\end{aligned}$$

(A17.a)

where $F_{jj'}^{(i,i')}=\frac{1}{Q}\sum_{q=1}^{Q}\frac{f_{qj}f_{qj'}}{M_q^{(i)}M_q^{(i')}}$. Then, the derivative with respect to $A_l^{(m)}$ is given by

$$\frac{\partial h_0}{\partial A_l^{(m)}}=\frac{1}{2}\sum_{i=1}^{I}\sum_{i'=1}^{I}\sum_{j=1}^{J}\sum_{j'=1}^{J}F_{jj'}^{(i,i')}p_i(\delta_{i,i'}-p_{i'})(A_{j'}^{(i')}\delta_{j,l}\delta_{i,m}+A_j^{(i)}\delta_{j',l}\delta_{i',m}).$$

(A17.b)

Since the matrix F is symmetric, i.e. $F_{jj'}^{(i,i')}=F_{j'j}^{(i',i)}$, we can interchange i with i' and j with j' resulting in

$$\frac{\partial h_0}{\partial A_l^{(m)}}=\frac{1}{2}\sum_{i=1}^{I}\sum_{i'=1}^{I}\sum_{j=1}^{J}\sum_{j'=1}^{J}F_{jj'}^{(i,i')}p_i(\delta_{i,i'}-p_{i'})2\delta_{j',l}\delta_{i',m}A_j^{(i)}=\sum_{i=1}^{I}\sum_{j=1}^{J}F_{jl}^{(i,m)}p_i(\delta_{i,m}-p_m)A_j^{(i)}.$$

(A18)

Since the derivative must vanish, after using the symmetry property of F we obtain:

$$\sum_{i=1}^{I}\sum_{j=1}^{J}F_{lj}^{(m,i)}p_i(\delta_{m,i}-p_m)A_j^{(i)}=0 \qquad \text{(A19)}$$

which completes the proof of Eq.(10). Eqs. (A15-19) have not been published before to the best of our knowledge.

A.4 Scaling of proton density values for all cubes

The objective function is given by Eq.(15):

$$\begin{aligned}
f(X)&=\tfrac{1}{Q}\sum_{q=1}^{Q}\tfrac{1}{2}\operatorname*{var}_k\tilde{C}_{qk}\\
&=\tfrac{1}{2Q}\sum_{q=1}^{Q}\operatorname*{var}_k\sum_{k'=1}^{I+J}C_{qk'}X_{k'k}\delta_{k'k}\\
&=\tfrac{1}{2Q}\sum_{q=1}^{Q}\operatorname*{var}_k C_{qk}x_k\\
&=\tfrac{1}{2Q}\sum_{q=1}^{Q}\left[\operatorname*{E}_k[(C_{qk}x_k)^2]-(\operatorname*{E}_k[C_{qk}x_k])^2\right],
\end{aligned} \qquad \text{(A20)}$$

where $E_k[v_k]$ is the expectation value of the random variable v_k. Since the matrix C contains only two non-zero values for each row q, we obtain explicitly

$$f(X)=\frac{1}{2Q}\sum_{q=1}^{Q}\left[\frac{1}{2}\sum_{k=1}^{I+J}(C_{qk}x_k)^2-\left(\frac{1}{2}\sum_{k=1}^{I+J}C_{qk}x_k\right)^2\right]=\frac{1}{4Q}\sum_{q=1}^{Q}\sum_{k=1}^{I+J}\sum_{m=1}^{I+J}\left[C_{qk}^2x_k^2\delta_{km}-\frac{1}{2}C_{qk}C_{qm}x_kx_m\right].$$

(A21)

Differentiation with respect to x_l yields

$$\frac{\partial f(X)}{\partial x_l}=\frac{1}{4Q}\sum_{q=1}^{Q}\sum_{k=1}^{I+J}\sum_{m=1}^{I+J}\left[C_{qk}^2 2x_k\delta_{km}\delta_{kl}-\frac{1}{2}C_{qk}C_{qm}(\delta_{kl}x_m+\delta_{ml}x_k\right]=\frac{1}{2Q}\sum_{q=1}^{Q}\sum_{k=1}^{I+J}C_{ql}(C_{ql}\delta_{kl}-\frac{1}{2}C_{qk})x_k.$$

(A22)

Since the derivative must vanish, we obtain the system of equations

$$\sum_{q=1}^{Q}\sum_{k=1}^{I+J}C_{ql}(C_{ql}\delta_{kl}-\tfrac{1}{2}C_{qk})x_k=0 \quad \text{for} \quad l=\{1,\ldots,I+J\}\ . \quad \text{(A23)}$$

Defining the matrix M with elements

$$M_{lk}=\sum_{q=1}^{Q}C_{ql}(C_{ql}\delta_{kl}-\frac{1}{2}C_{qk}) \quad \text{(A24)}$$

gives the equation

$$\sum_{k=1}^{I+J}M_{lk}x_k=0 \quad \text{for} \quad l=\{1,\ldots,I+J\}\ . \quad \text{(A25)}$$

Since one of the unknowns can be specified to be one, i.e. $x_1 = 1$, the system of equations can be solved for the remaining unknowns by matrix inversion leading to the results in Eq. (19). This approach (Eqs. (A20-A25)) has not been published before to the best of our knowledge.

Dietmar Cordes received the B.S. and M.S. degree in Physics from the Technical University of Clausthal, Germany, in 1981 and 1985, respectively, and in 1989 a Ph.D.

degree in Theoretical Physics from the University of Nevada, Reno. He then joined the University of Wisconsin-Madison for a 4-year program in medical physics with focus on MRI and functional MRI (fMRI). His research interests include MR physics, MR imaging and data analysis in fMRI. He is currently the Director of Neuroimaging at the Cleveland Clinic Lou Ruvo Center for Brain Health in Las Vegas, NV, USA.

References

Abbas Z, Gras V, Mollenhoff K, Keil F, Oros-Peusqueens A, Shah NJ. Analysis of Proton-Density Bias Corrections Based on T_1 Measurement for Robust Quantification of Water Content in the Brain at 3 Tesla. Magnetic Resonance in Medicine. 2014; 72:1735–1745. [PubMed: 24436248]

Ajata C, Ropper AH. Ischaemic brain edema. Journal of Clinical Neuroscience. 2002; 9(2):113–124. [PubMed: 11922696]

Andersen C. In vivo estimation of water content in cerebral white matter of brain tumour patients and normal individuals: towards a quantitative brain oedema definition. Acta Neurochir (Wien). 1997; 139:249–255. discussion 255–246. [PubMed: 9143593]

Ashburner J, Friston KJ. Unified Segmentation. NeuroImage. 2005; 26:839–851. [PubMed: 15955494]

Bakker CG, DeGraaf CN, VanDijk P. Restoration of signal polarity in a set of inversion recovery NMR images. IEEE Trans Med Imaging. 1984; 3:197–202. [PubMed: 18234630]

Barral JK, Gudmundson E, Stikov N, Etezadi-Amoli M, Stoica P, Nishimura DG. A Robust Methodology for in Vivo T_1 Mapping. Magnetic Resonance in Medicine. 2010; 64:1057–1067. [PubMed: 20564597]

Baudrexel S, Reitz SC, Hof S, Gracien RM, Fleischer V, Zimmermann H, Droby A, Klein JC, Deichmann R. Quantitative T1 and proton density mapping with direct calculation of radiofrequency coil transmit and receive profiles from two-point variable flip angle data. NMR in Biomedicine. 2015; 29:349–360.

Cordes, D., Zhuang, X., Sreenivasan, K., Hua, Le, H. Organization for Human Brain Mapping Conference Proceedings (HBM). Vol. 6825. Hawaii: 2015. Estimation of Receiver Coil Sensitivities for Quantification of Proton Density.

Cordes, D., Zhuang, X., Sreenivasan, K., Hua, Le, H. International Society for Magnetic Resonance in Medicine (ISMRM) Annual Conference Proceedings. Singapore: 2016. Simultaneous Estimation of Proton Densities and Receiver Coil Sensitivities using Optimized Basis Functions; p. 1896

Fatouras PP, Marmarou A. Use of magnetic resonance imaging for in vivo measurements of water content in human brain: method and normal values. J Neurosurg. 1999; 90:109–115.

Fatouras PP, Marmarou A, Kraft KA, Inao S, Schwarz FP. In vivo brain water determination by T_1 measurements-effect of total water-content, hydration fraction, and field strength. Magn Reson Med. 1991; 17:402–413. [PubMed: 2062213]

Gelman N, Ewing JR, Gorell JM, Spickler EM, Solomon EG. Interregional variation of longitudinal relaxation rates in human brain at 3.0T: relation to estimated iron and water contents. Magn Reson Med. 2001; 45:71–79. [PubMed: 11146488]

Gudbjartsson H, Patz S. The Rician Distribution of Noisy MRI Data. Magnetic Resonance in Medicine. 1995; 34(6):910–914. [PubMed: 8598820]

Jolliffe, IT. Principal Component Analysis. 2nd. Springer; 2002.

Jurcoane A, Wagner M, Schmidt C, Mayer C, Gracien RM, Hirschmann M, Deichmann R, Volz S, Ziemann U, Hattingen E. Within-Lesion Differences in Quantitative MRI Parameters Predict Contrast Enhancement in Multiple Sclerosis. Journal of Magnetic Resonance Imaging. 2013; 38:1454–1461. [PubMed: 23554005]

Kettenring JR. Canonical analysis of several sets of variables. Biometrika. 1971; 58:433–451.

Laule C, Vavasour IM, Moore GR, Oger J, Li DK, Paty DW, MacKay AL. Water content and myelin water fraction in multiple sclerosis. A T2 relaxation study. J Neurol. 2004; 251:284–293. [PubMed: 15015007]

Laule C, Leung E, Lis DK, Traboulsee AL, Paty DW, MacKay AL, Moore GR. Myelin water imaging in multiple sclerosis: quantitative correlations with histopathology. Mult Scler. 2006; 12:747–753. [PubMed: 17263002]

Li YO, Adali T, Wang W, Calhoun VD. Joint Blind Source Separation by Multiset Canonical Correlation Analysis. IEEE Trans Signal Process. 2009; 57:3918–3929. [PubMed: 20221319]

Mezer A, Yeatman JD, Stikov N, Kay KN, Cho NJ, Doughterty RF, Perry ML, Parvizi J, Hua LH, Butts-Pauly K, Wandell BA. Quantifying the local tissue volume and composition in individual brains with magnetic resonance imaging. Nature Medicine. 2013; 19:1667–1672.

Mezer A, Rokem A, Berman S, Hastie T, Wandell BA. Evaluating Quantitative Proton-Density-Mapping Methods. Human Brain Mapping. 2016; 37(10):3623–3635. [PubMed: 27273015]

Neeb H, Shah NJ. Enhancing the precision of quantitative water content mapping by optimizing sequence parameters. Magn Reson Med. 2006; 56:224–229. [PubMed: 16732595]

Neeb H, Zilles K, Shah NJ. A new method for fast quantitative mapping of absolute water content in vivo. NeuroImage. 2006; 31:1156–1168. [PubMed: 16650780]

Neeb H, Ermer V, Stocker T, Shah NJ. Fast quantitative mapping of absolute water content with full brain coverage. NeuroImage. 2008; 42:1094–1109. [PubMed: 18632287]

Nocedal, J., Wright, SJ. Numerical Optimization. Springer Verlag New York, Inc; 1999.

Oros-Peusquens AM, Keil F, Langen KJ, Herzog H, Stoffels G, Weiss C, Shah NJ. Fast and accurate water content and T2 mapping in brain tumours localised with FET-PET. Nucl Inst Methods Phys Res. 2014; A734:185–190.

Preibisch C, Deichmann R. Influence of RF Spoiling on the Stabiloity and Accuracy of T1 Mapping Based on Spoiled FLASH with Varying Flip Angles. Magnetic Resonance in Medicine. 2009; 61:125–135. [PubMed: 19097220]

Schmidt P, Gaser C, Arsic M, Buck D, Förschler A, Berthele A, Hoshi M, Ilg R, Schmid VJ, Zimmer C, Hemmer B, Mühlau M. An automated tool for detection of FLAIR-hyperintense white-matter lesions in Multiple Sclerosis. NeuroImage. 2012; 59:3774–3783. [PubMed: 22119648]

Shah NJ, Neeb H, Zaitsev M, Steinhoff S, Kircheis G, Amunts K, Haussinger D, Zilles K. Quantitative T1 mapping of hepatic encephalopathy using magnetic resonance imaging. Hepatology. 2003; 38:1219–1226. [PubMed: 14578860]

Shah NJ, Neeb H, Kircheis G, Engels P, Haussinger D, Zilles K. Quantitative cerebral water content mapping in hepatic encephalopathy. NeuroImage. 2008; 41:706–717. [PubMed: 18456518]

Stikov N, Boudreau M, Levesque IR, Tardif CL, Barral JK, Pike GB. On the Accuracy of T_1 Mapping: Searching for Common Ground. Magnetic Resonance in Medicine. 2015; 73:514–522. [PubMed: 24578189]

Volz S, Nöth U, Deichmann R. Correction of Systematic Errors in Quantitative Proton Density Mapping. Magnetic Resonance in Medicine. 2012a; 68:74–85. [PubMed: 22144171]

Volz S, Nöth U, Jurcoane A, Ziemann U, Hattingen E, Deichmann R. Quantitative proton density mapping: correcting the receiver sensitivity bias via pseudo proton densities. NeuroImage. 2012b; 63:540–552. [PubMed: 22796988]

Wang J, Qiu M, Kim H, Constable RT. T_1 Measurements incorporating flip angle calibration and correction in vivo. Journal of Magnetic Resonance. 2006; 182:283–292. [PubMed: 16875852]

Warntjes JBM, Dahlqvist O, Lundberg P. Novel method for rapid, simultaneous T1, T2(*), and proton density quantification. Magn Reson Med. 2007; 57:528–537. [PubMed: 17326183]

Weiskopf N, Lutti A, Helms G, Novak M, Ashburner J, Hutton C. Unified Segmentation based correction of R1 brain maps for RF transmit field in homogeneities (UNICORT). NeuroImage. 2011; 54(3):2116–2124. [PubMed: 20965260]

Biographies

Zhengshi Yang received the B.S. degree in Physics from Huazhong University of Science and Technology, Wuhan, China, in 2013 and the M.S. degree in Physics from University of Kentucky, Lexington, United States in 2015. Currently, he is a research engineer at the

Cleveland Clinic Lou Ruvo Center for Brain Health in Las Vegas, United States. His research interests include multivariate mathematical modeling and MRI image analysis.

Xiaowei Zhuang received the B.S. degree in Biomedical Engineering from Jiaotong University, Beijing, China, in 2012 and the M.S. degree in Biomedical Engineering from University of Southern California, Los Angeles, United States, in 2014. Currently, she is a research engineer at the Cleveland Clinic Lou Ruvo Center for Brain Health in Las Vegas, United States. Her research interests include MRI image analysis and machine learning.

Karthik Ramakrishnan Sreenivasan received the M.S. degree in Electrical Engineering from Auburn University, Alabama, USA. He is currently a research engineer at the Cleveland Clinic Lou Ruvo Center for Brain Health in Las Vegas, Nevada, USA. His research interests include signal and image processing, investigation of brain connectivity using Functional Magnetic Resonance Imaging (fMRI) data, analysis of Positron Emission Tomography (PET) imaging data, and using machine learning approaches for brain state classification.

Virendra Radheshyam Mishra received the Ph.D. degree in Biomedical Engineering from joint universities of The University of Texas at Southwestern Medical Center at Dallas and The University of Texas at Arlington, Texas, USA and M. S. degree in Electrical Engineering from The University of Texas at Arlington, Texas, USA. He is currently a staff member at the Cleveland Clinic Lou Ruvo Center for Brain Health in Las Vegas, Nevada, USA. His research interests include image and signal processing of diffusion MRI and pseudo-continuous arterial spin labeling MRI data and predicting imaging biomarkers using machine learning techniques in clinical populations.

Le H. Hua received the M.D. degree from the Keck School of Medicine at University of Southern California in Los Angeles, CA, USA in 2008. She completed her Neurology residency at Stanford University, Stanford, CA, USA, in 2012 and completed a fellowship in Neuro-Immunology and Multiple Sclerosis from Barrow Neurological Institute in Phoenix, AZ, USA, in 2013. She is currently a physician at the Cleveland Clinic Lou Ruvo Center for Brain Health in Las Vegas, NV, USA, and oversees the Multiple Sclerosis Clinical and Research Programs.

Highlights

- Proton density is computed using multi-channel coil data.
- New basis functions are developed using a family of functions whose proton density have an inverse linear relationship to the T_1 value.
- The proton density problem is solved using purely linear algebraic equations.

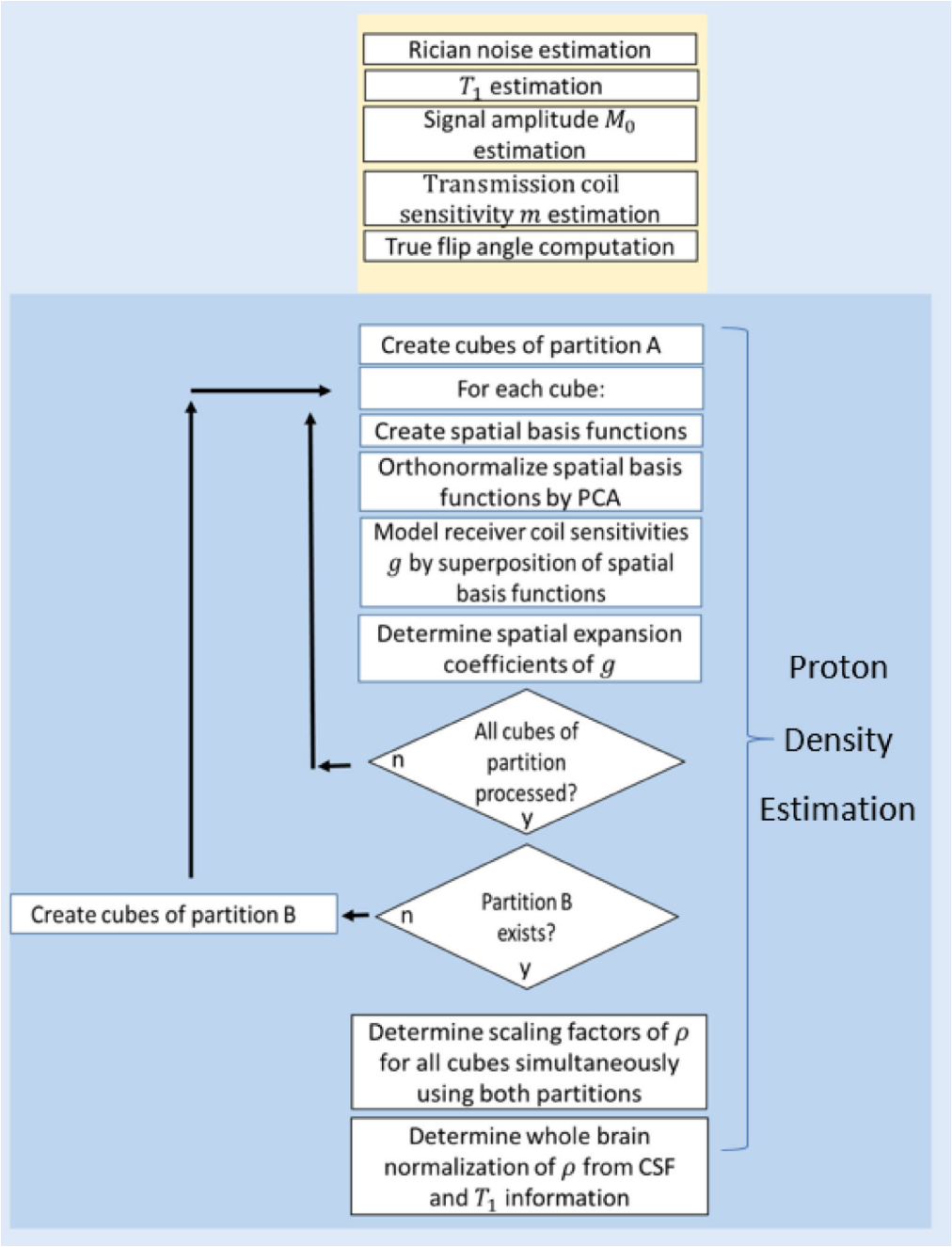

Fig.1.

Flow chart showing the proposed analysis steps. The novelty of our approach is how the transmission coil sensitivity is estimated, the spatial basis functions are created and used to model the receiver coil sensitivities, the spatial expansion coefficients of g are calculated, and the scaling factors of the proton density are determined simultaneously for all cubes in one step.

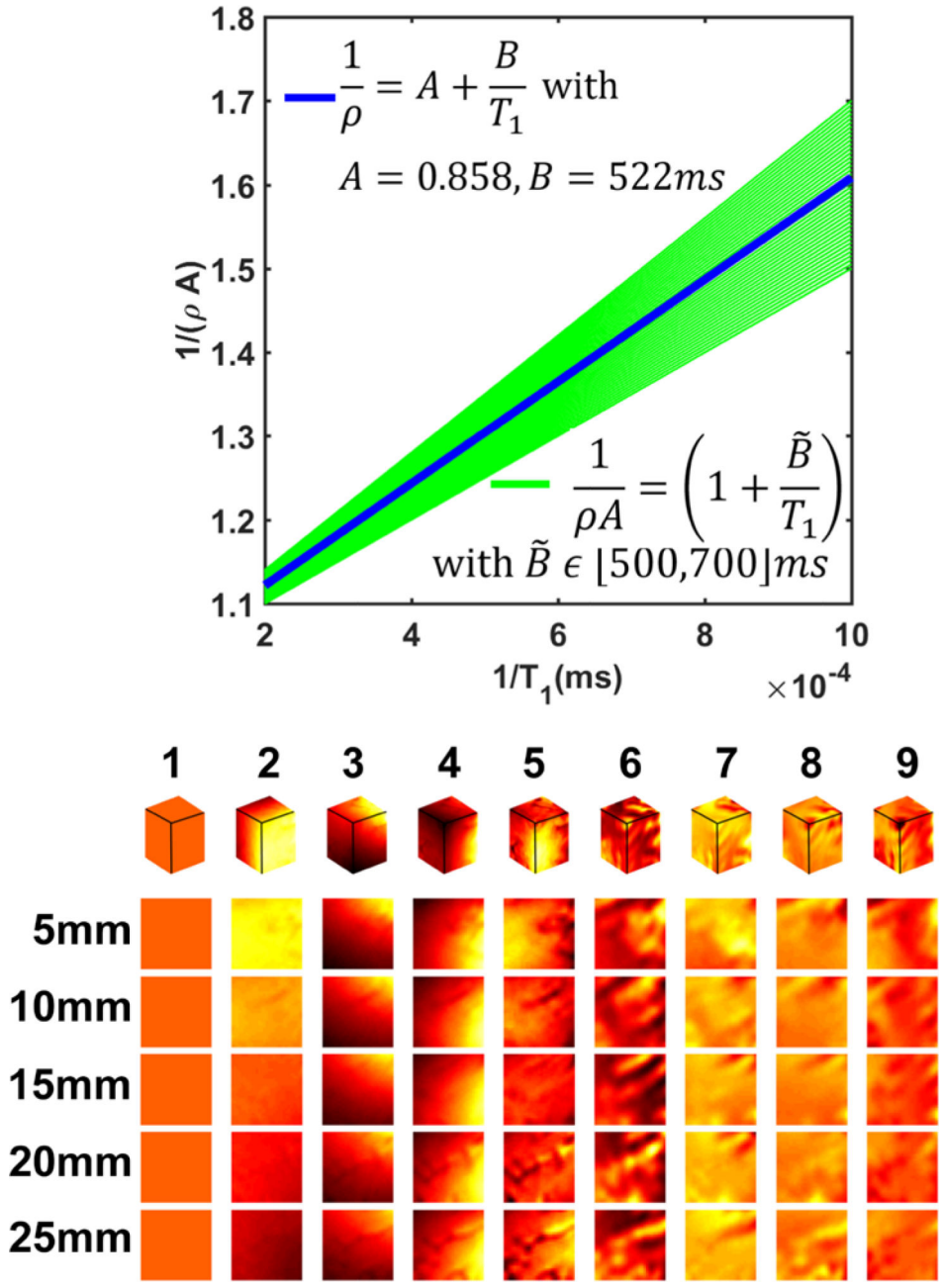

Fig.2.

Top: Inverse linear relationship between proton density ρ and T_1 for a single parameter {A, B} (blue line) and for a family of parameters from which the novel basis functions are derived (green lines covering an entire area). Bottom: First nine spatial basis functions derived after PCA orthonormalization for a cube (30mm × 30mm × 30mm) in white matter. A 3D view of each basis function is shown as well as five 2D-slices of each basis function at indicated distances from the right front face. The first basis function represents a constant. All the other basis functions are orthonormal over the cube. For the nearest coil (coil 1), dominant contributions are from functions 1, 2, 3 and 4 whereas for the other more distant

coils, main contributions are from functions 1, 2, 3. Functions 5 to 9 also contribute but have a weight that is about one magnitude smaller.

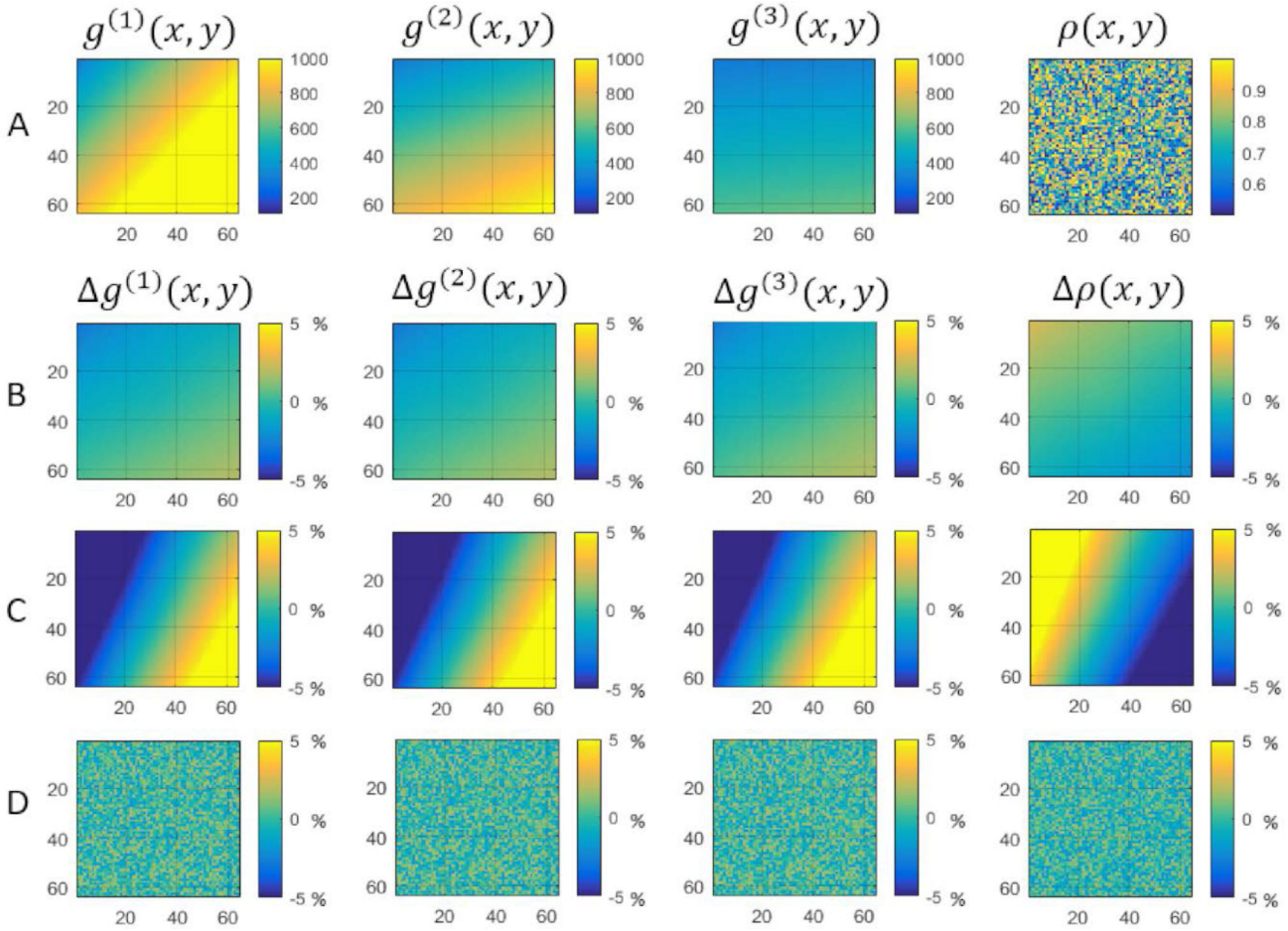

Fig.3.

2D noiseless toy example involving 3 coils on a 64×64 pixel grid and error obtained in recovering the images from the signal equation (Eq.(3)) for three different methods. The coil sensitivities contain a mixture of polynomials up to 2nd order using 6 functions {const, x, y, xy, x^2, y^2} and an additional 2D Gaussian function (amplitude 30, centered at $x = y = 32$, standard deviation $\sigma = 40$). The proton density is a uniform random image with values $0.5 < \rho(x, y) < 1$. A corresponding T_1 image satisfying the inverse linear relationship $\frac{1}{\rho} = 0.879 + \frac{503\text{ms}}{T_1}$ was also generated. The signal amplitudes for all coils were computed according to Eq.(3). A. Simulated coil sensitivities $g^{(1,2,3)}(x,y)$ and proton density $\rho(x,y)$. B. Error $\Delta g^{(1,2,3)} = g^{(1,2,3)}$(ground truth) − $g^{(1,2,3)}$(estimated) and $\Delta\rho = \rho$(ground truth) − ρ(estimated) obtained using a polynomial basis up to 2nd order {const, x, y, xy, x^2, y^2} in the modeling of the coil sensitivities. C. Error $\Delta g^{(1,2,3)} = g^{(1,2,3)}$(ground truth) – $g^{(1,2,3)}$(estimated) and $\Delta\rho = \rho$(ground truth) − ρ(estimated) obtained using a polynomial basis up to 3rd order with 8 functions {const, x, y, xy, x^2, y^2, x^3, y^3}. D. Error $\Delta g^{(1,2,3)} = g^{(1,2,3)}$(ground truth) − $g^{(1,2,3)}$(estimated) and $\Delta\rho = \rho$(ground truth) − ρ(estimated) obtained using the proposed optimized basis set similar to the ones in Fig.2 except for the 2D case.

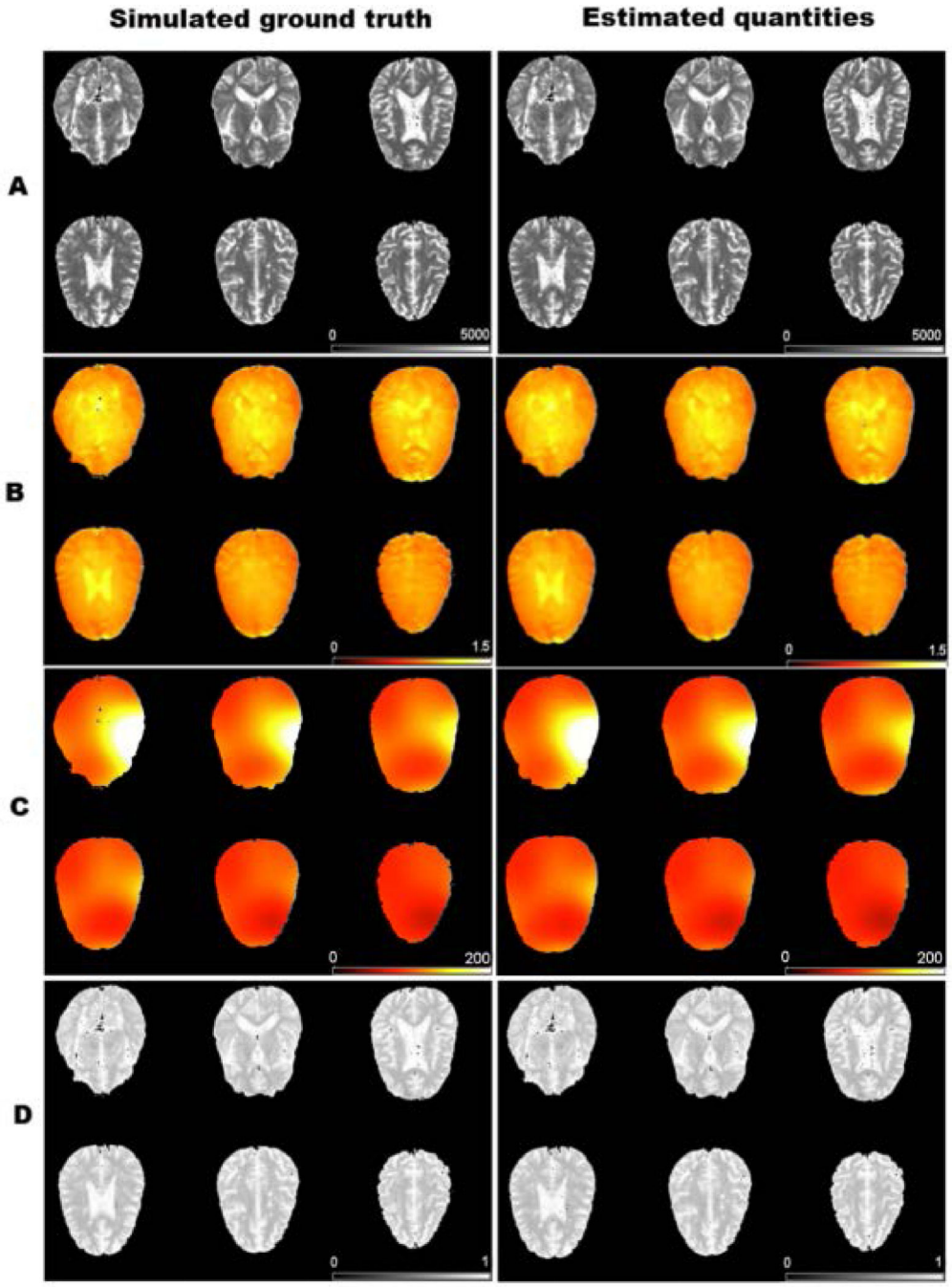

Fig.4.

Images of simulated (left) and estimated (right) MR quantities. From top to bottom: A. longitudinal relaxation rate T_1 (units are ms), B. observed transmission coil sensitivity m, C. receiver coil sensitivity $g^{(i)}$ of one arbitrary chosen coil element, D. proton density ρ.

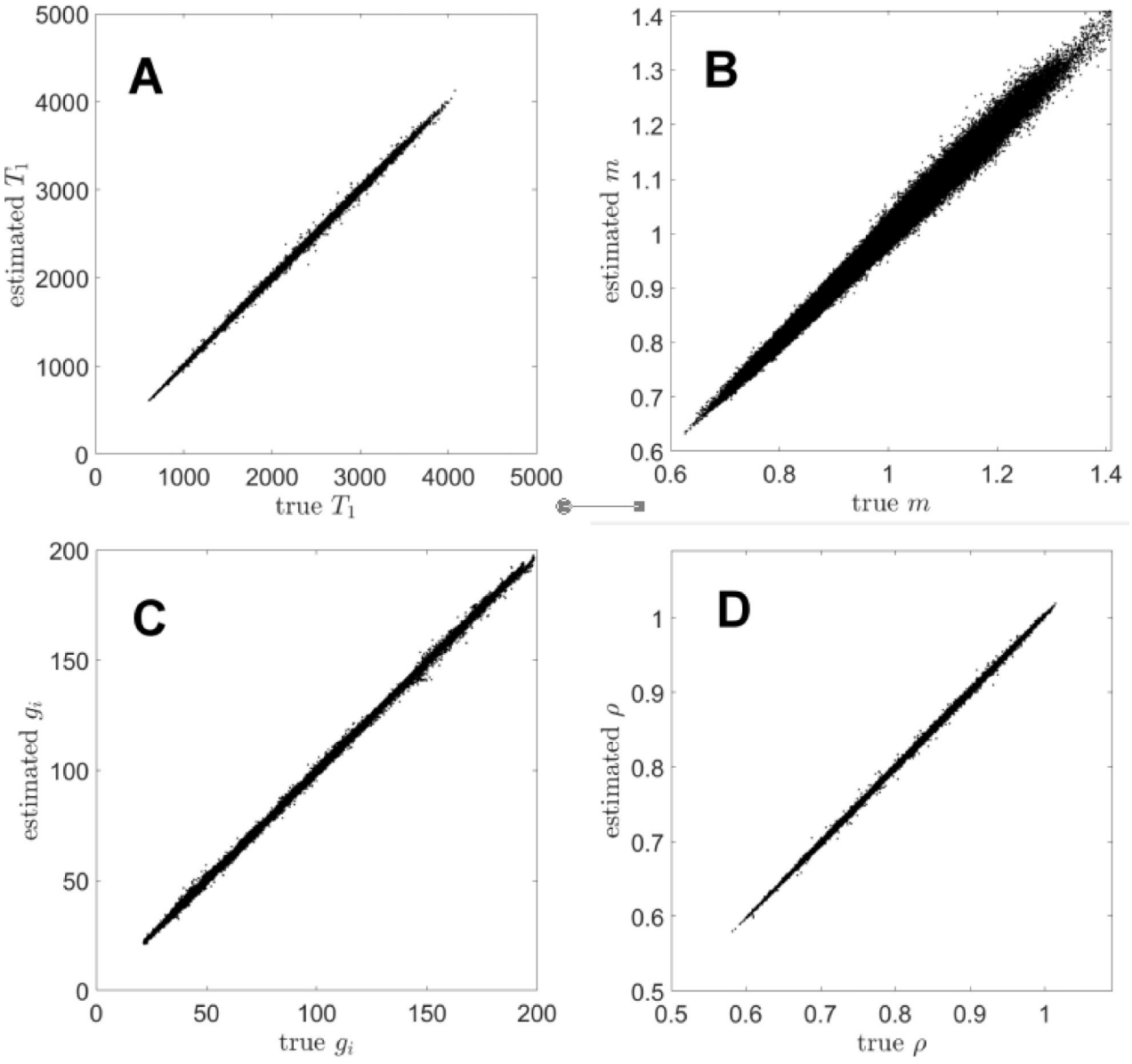

Fig.5.

Estimation accuracy of simulation: A. longitudinal relaxation rate T_1 (in ms), B. observed transmission coil sensitivity m, C. receiver coil sensitivity $g^{(i)}$ averaged over all coil elements, D. proton density ρ.

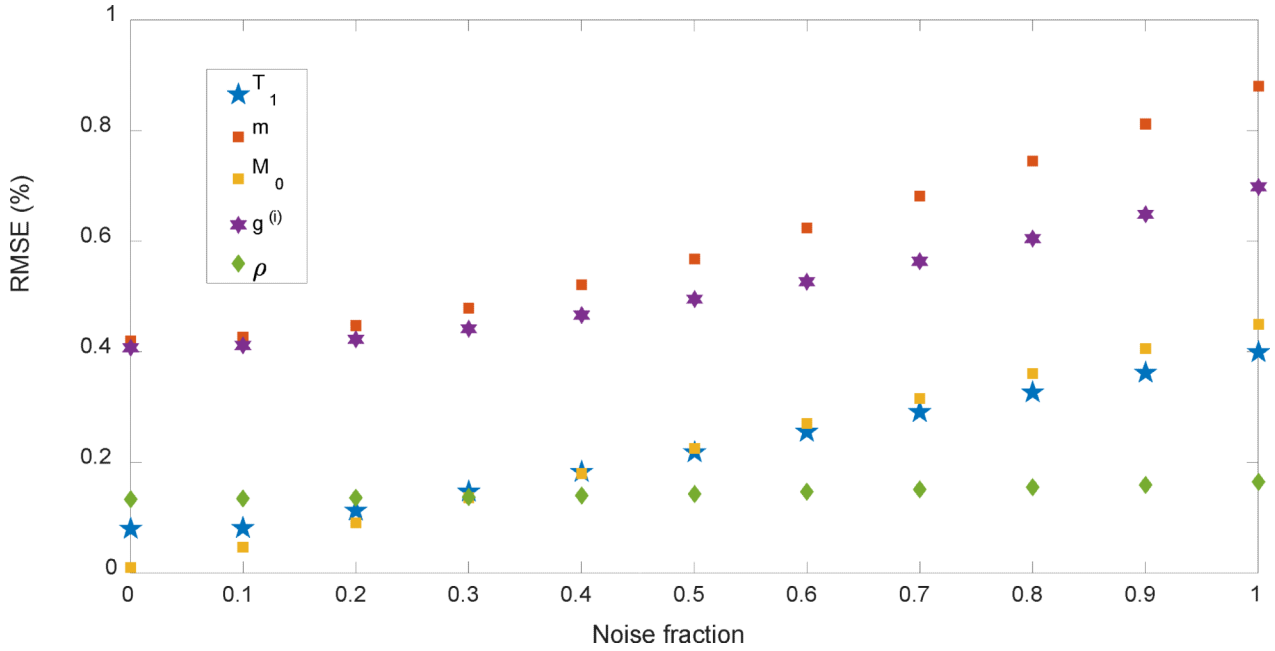

Fig.6.

Root-mean-square error (RMSE) in % of the estimation accuracy for longitudinal relaxation rate T_1, transmission coil sensitivity m, signal amplitude M_0, receiver coil sensitivity $g^{(i)}$ (averaged over all 32 coil elements) and proton density ρ, using simulated data with different noise fractions. A noise fraction of 0 indicates no noise added and a noise fraction of 1 indicates the same noise level as estimated from real MRI data. The overall error for all estimated quantities is less than 1 %. The small bias at zero noise fraction is due to partial volume effects introduced by the coregistration step of all generated images. Note that the noise sensitivity of ρ is by a factor of about 0.4 smaller than the noise sensitivity of T_1.

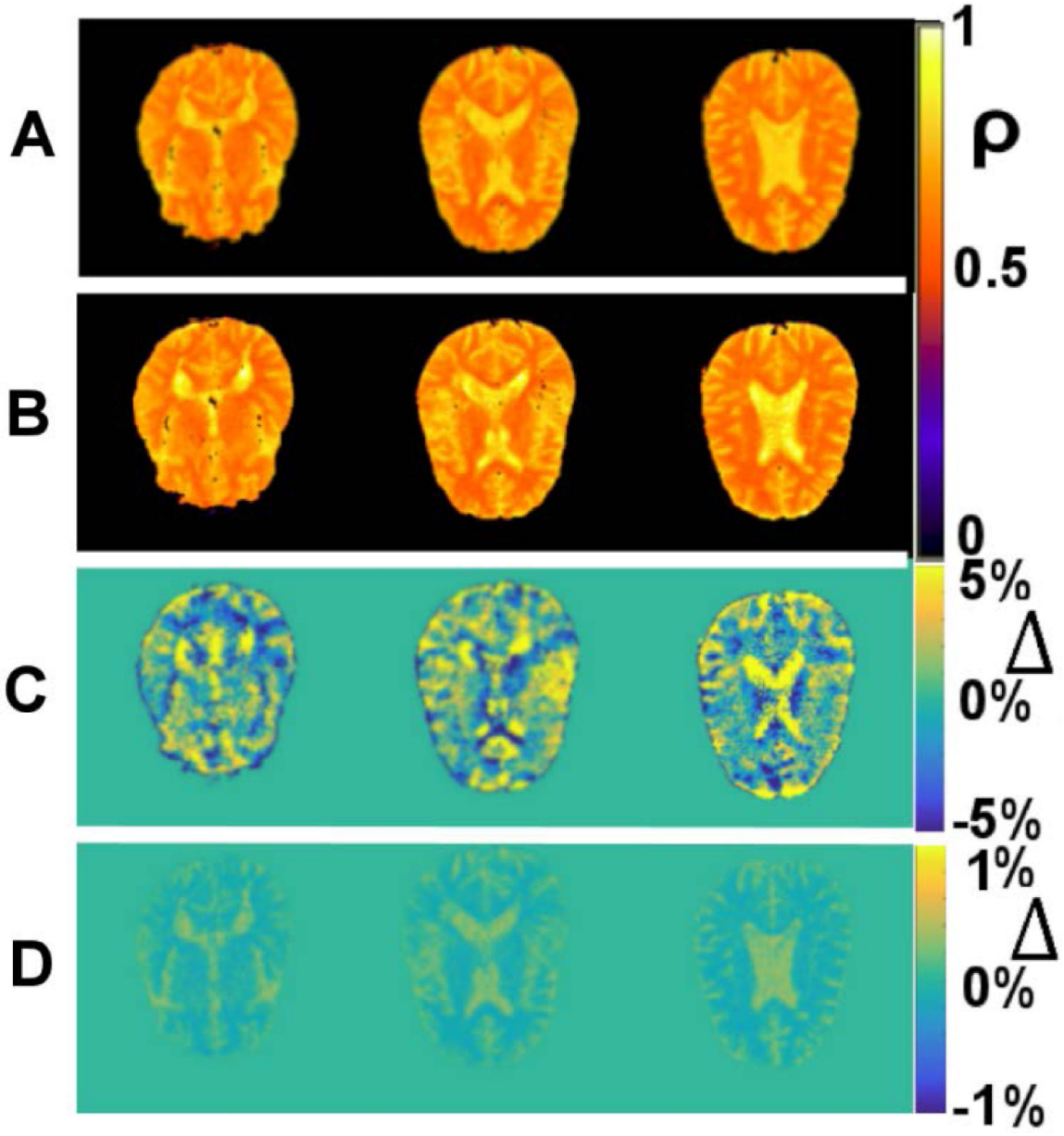

Fig.7.

Comparison of proton density results using a numerical brain phantom. A. Ground truth images of proton density. B. Results obtained using the method by Mezer et al. (2016) rescaled so that the mean proton density is the same as in the ground truth images. C. Difference map $\rho(B) - \rho(A)$ in percent. D. Percent difference map between the images obtained by the proposed method (this research) and the ground truth in A. Note the difference in scale between C and D.

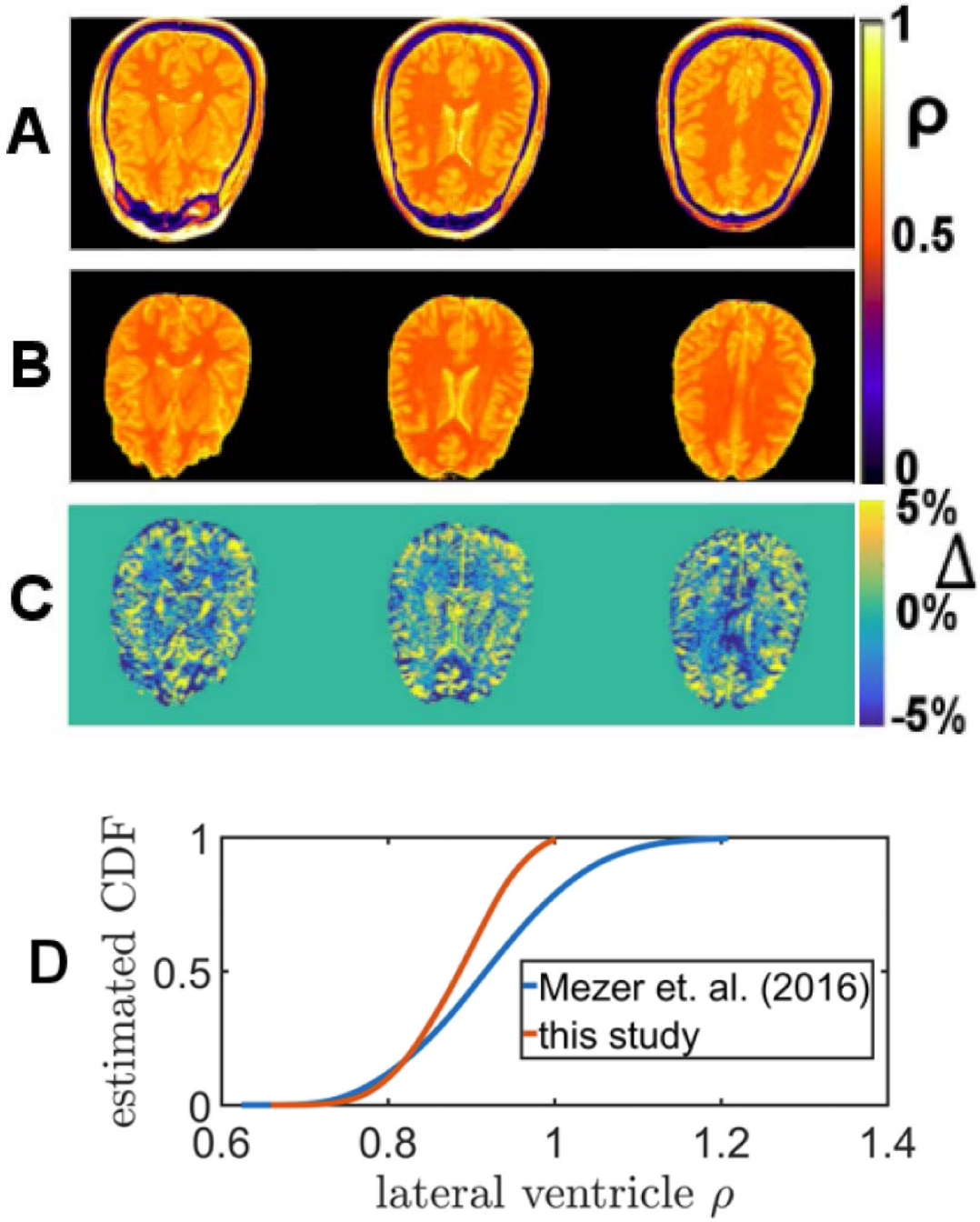

Fig.8.

Proton density results using public data for a normal subject from Mezer et al. (2016). A. Scaled proton density map results according to Mezer et al. (2016) B. Proton density map obtained using the proposed method (this study). The images in A were scaled so that the mean proton density is the same as in B. C. Difference map $\rho(A) - \rho(B)$ in percent. D. Effect of CSF normalization using the final proton density images with no scaling involved for the images obtained by the method of Mezer et al. (2016) and the proposed method. Here, none of the proton density images were mean adjusted. The vertical axis shows the

empirical cumulative density function (CDF) for the proton density in the lateral ventricles segmented by FreeSurfer. Note that 20% of voxels have a $\rho > 1$ using the method by Mezer et al. (blue curve) whereas for the proposed method $\max(\rho) = 1$ (red curve).

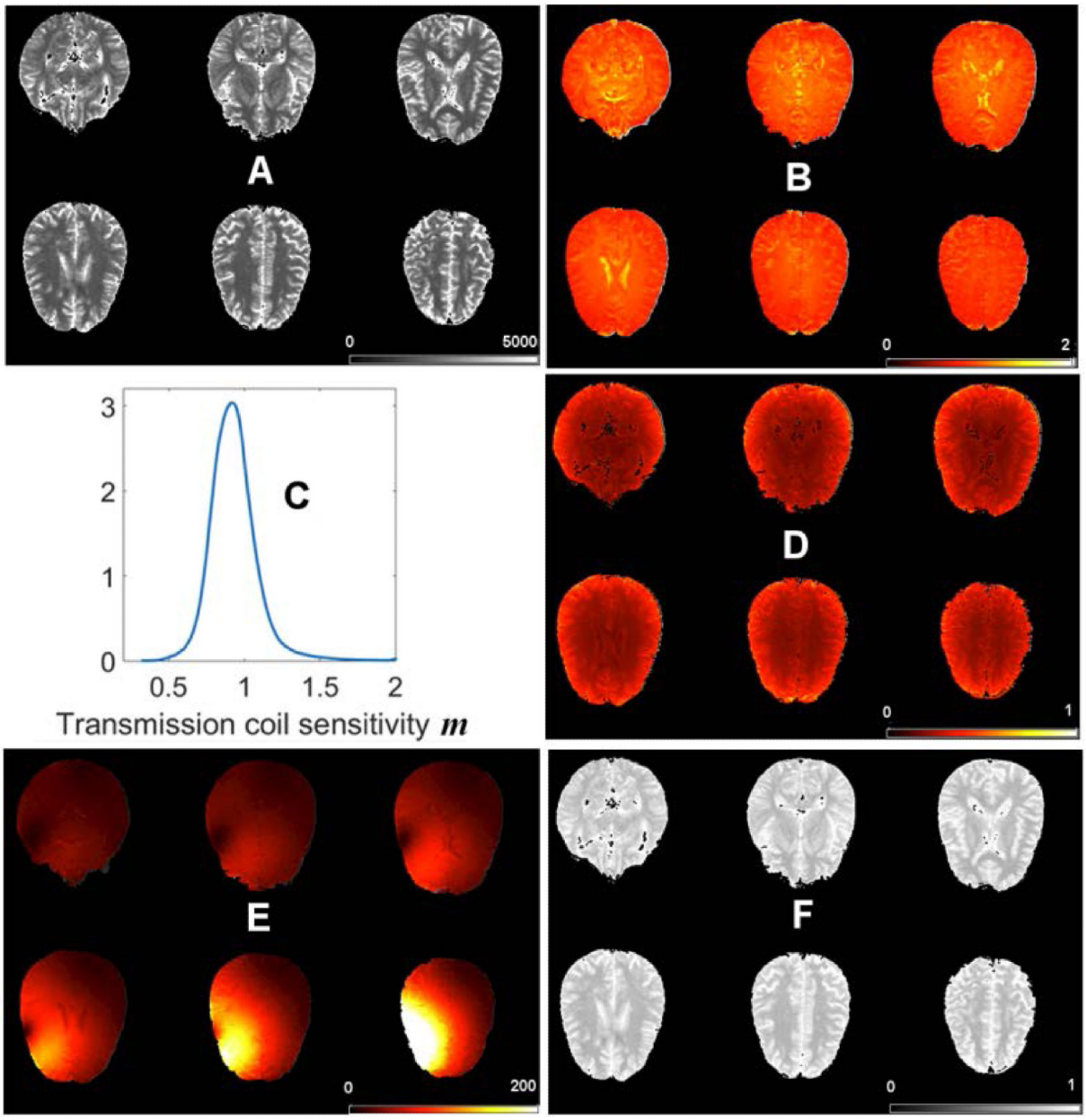

Fig. 9.

Estimated images of a representative subject (subject 1): A. longitudinal relaxation time T_1, B. observed transmission coil sensitivity m, C. kernel-density estimate of the distribution of the observed transmission coil sensitivity m, D. signal amplitude M_0, E. receiver coil sensitivity $g^{(i)}$ of one arbitrary chosen coil element, F final proton density ρ after normalization.

Table 1

Root-Mean-Square Error (RMSE) of estimated T_1, observed transmission coil sensitivity m, receiver coil sensitivity g and proton density ρ for different simulated data.

Simulation	Optimized basis functions	T_1	m	g	ρ
$\mathrm{RMSE}\frac{1}{\rho}=0.858+\frac{522\mathrm{ms}}{T_1}$, $\tilde{B}=608ms$	$\tilde{B}\in$ [500,700]ms	0.4%	0.8%	0.7%	<0.2%
$\mathrm{RMSE}\frac{1}{\rho}=0.858+\frac{422\mathrm{ms}}{T_1}$, $\tilde{B}=492ms$	$\tilde{B}\in$ [500,700]ms	0.4%	0.8%	1.7%	1.4%
$\mathrm{RMSE}\frac{1}{\rho}=0.858+\frac{522\mathrm{ms}}{T_1}+\frac{\frac{1}{2}(522\mathrm{ms})^2}{(T_1)^2}$	$\tilde{B}\in$ [500,700]ms	0.4%	0.8%	2.9%	2.5%

Table 2

Root-Mean-Square Error (RMSE) of estimated proton density ρ using the SPM12 segmentation toolbox for simulated data with $\frac{1}{\rho}=0.858+\frac{522\text{ms}}{T_1}$, $\tilde{B}=608ms$ as a function of regularization parameter and FWHM. The error rate for the receiver coil sensitivity (not shown) is of the same order.

Regularization / **FWHM (mm)**	**0**	**10^{-5}**	**10^{-4}**	**10^{-3}**	**10^{-2}**
50	9.9%	8.3%	7.5%	7.1%	7.6%
60	8.6%	7.8%	7.2%	6.6%	7.3%
70	8.5%	7.4%	6.5%	6.1%	8.1%
80	7.8%	6.7%	5.9%	5.7%	9.3%
90	7.8%	6.2%	5.6%	6.2%	10.6%
100	8.1%	6.6%	5.4%	6.9%	11.5%
110	8.1%	5.8%	4.9%	8.0%	12.1%
120	5.0%	4.3%	5.3%	9.3%	12.6%
130	5.0%	4.1%	6.6%	10.3%	12.9%
140	6.1%	6.3%	8.2%	11.1%	13.1%

Med Image Anal. Author manuscript; available in PMC 2018 August 01.

Table 3

Estimated values for A and B such that $\frac{1}{\rho}=A+\frac{B}{T_1}$ for different analysis methods for simulated data[1].

	Gray Matter		White Matter		Whole Brain		Whole Brain	Whole Brain
Method	**A**	**B (ms)**	**A**	**B (ms)**	**A**	**B (ms)**	**RMSE *g***	**RMSE *ρ***
optimized basis functions	0.8403	522.13	0.8403	522.15	0.8403	522.14	0.7%	<0.2%
bias field estimation using SPM12	0.8834	484.74	0.8785	508.09	0.8555	528.13	3.2%	4.1%

[1]Simulated whole brain data were generated according to the model $\frac{1}{\rho}=0.858+\frac{522\text{ms}}{T_1}$.

Table 4

A and B values such that $\frac{1}{\rho}=A+\frac{B}{T_1}$ for 9 MS subjects and 1 healthy subject (#hs).

	Gray Matter		White Matter		Lesion[1]		Whole Brain		WM - Lesion	
Subject	**A**	**B (ms)**	**A**	**B (ms)**	**A**	**B (ms)**	**A**	**B (ms)**	**A**	**B (ms)**
#1	0.8761	544.31	0.8761	544.29	0.8760	544.35	0.8761	544.29	4.74×10^{-05}	-0.06
#2	0.8621	535.60	0.8621	535.62	0.8621	535.65	0.8621	535.60	1.90×10^{-05}	-0.03
#3	0.8752	543.79	0.8752	543.84	0.8751	543.91	0.8752	543.81	5.33×10^{-05}	-0.06
#4	0.8741	543.03	0.8741	543.06	0.8741	543.08	0.8741	543.04	2.12×10^{-05}	-0.02
#5	0.8723	541.92	0.8723	541.95	0.8723	541.94	0.8723	541.92	-7.69×10^{-07}	0.01
#6	0.8684	539.51	0.8684	539.54	0.8682	539.71	0.8684	539.51	1.45×10^{-04}	-0.17
#7	0.8739	542.92	0.8738	542.98	0.8738	543.07	0.8739	542.95	7.16×10^{-05}	-0.09
#8	0.8677	539.12	0.8677	539.14	0.8676	539.18	0.8677	539.13	3.10×10^{-05}	-0.04
#9	0.8683	539.50	0.8683	539.52	0.8683	539.54	0.8683	539.49	1.31×10^{-05}	-0.02
#hs	0.8609	534.99	0.8609	534.98	NA	NA	0.8609	534.97	NA	NA

[1]Note: Lesion identification was done using the method of Schmidt et al., 2012.

Table 5

Mean T_1 (in ms) and ρ values in selected brain regions for all subjects.

		GM	Left Caudate	Left Putamen	Right Caudate	Right Putamen	WM	Lesion
#1	T_1	1657	1349	1227	1438	1246	1209	1382
#1	ρ	0.81	0.78	0.76	0.79	0.76	0.74	0.78
#2	T_1	1557	1379	1242	1410	1219	1088	1261
#2	ρ	0.82	0.79	0.77	0.79	0.78	0.73	0.77
#3	T_1	1524	1543	1291	1493	1302	1066	1257
#3	ρ	0.80	0.81	0.77	0.80	0.77	0.72	0.75
#4	T_1	1630	1476	1269	1465	1315	1146	1438
#4	ρ	0.81	0.80	0.77	0.79	0.77	0.73	0.79
#5	T_1	1577	1428	1289	1402	1295	1094	1356
#5	ρ	0.81	0.79	0.77	0.79	0.77	0.72	0.78
#6	T_1	1564	1451	1241	1404	1266	1105	1020
#6	ρ	0.81	0.80	0.77	0.79	0.77	0.73	0.72
#7	T_1	1587	1336	1264	1365	1335	1045	1557
#7	ρ	0.80	0.77	0.76	0.78	0.77	0.71	0.79
#8	T_1	1523	1345	1197	1425	1187	1113	1293
#8	ρ	0.81	0.78	0.76	0.79	0.75	0.73	0.77
#9	T_1	1551	1405	1232	1423	1240	1116	1362
#9	ρ	0.81	0.79	0.76	0.79	0.77	0.73	0.79
avg±std	T_1	1574±45	1412±69	1250±31	1425±37	1267±49	1109±48	1325±148
avg±std	ρ	0.809±0.005	0.791±0.011	0.764±0.006	0.794±0.006	0.768±0.007	0.728±0.011	0.769±0.023
#hs	T_1	1490	1324	1228	1382	1241	1018	NA
#hs	ρ	0.81	0.78	0.77	0.79	0.77	0.71	NA

Note: The abbreviation “hs” indicates the healthy subject.

Table 6

Comparison of proton density values with values from literature.

	This study (hs)	This study (MS)	Volz et al. (2012a)	Volz et al. (2012b)	Neeb et al. (2008)	Warntjes et al. (2007)	Fatouras et al. (1999)
GM	0.810	0.809±0.0055	0.811±0.010	0.810±0.010	0.812±0.012	-	-
L Caudate	0.785	0.791±0.011	-		-	-	-
R Caudate	0.796	0.794±0.0062	-		-	-	-
Caudate head	0.791	0.795±0.0071	0.815±0.010	0.802±0.007	0.848±0.017	0.813	0.803
L Putamen	0.769	0.764±0.0059	-		-	-	-
R Putamen	0.772	0.768±0.007	-		-	-	-
Putamen	0.771	0.766±0.0059	0.819±0.011	0.798±0.013	0.832±0.017	0.823	-
WM	0.715	0.728±0.011	0.703±0.015	0.697±0.013	0.709±0.011	-	-